FERMILAB-Pub-03/355-E

CDF Central Outer Tracker

T. Affolder,[g] D. Allspach,[c] D. Ambrose,[j] J. Bialek,[e] W. Bokhari,[j] M. Brozovic,[b] M. Binkley,[c] K. Burkett,[d] A. Byon-Wagner,[c] F. Cogswell,[e] N. Dressnandt,[j] Z. Feng,[f] M. Franklin,[d] L. Galtieri,[g] D. W. Gerdes,[f,h] J. Greenwood,[c] V. Guarino,[a] J. Guimaraes da Costa,[f,h,d] R. Haggerty,[d] C. Hall,[d] J. Heinrich,[j] A. Holloway,[d] T. Jacobi,[d] K. Kephart,[c] D. Khazins,[b,c] Y. K. Kim,[g] M. Kirby,[b] W. Kononenko,[j] A. V. Kotwal,[b] J. Kraus,[e] T. M. Liss,[e] N. Lockyer,[j] R. Madrak,[d] T. Miao,[c] A. Mukherjee,[c] C. Neu,[e] M. Newcomer,[j] J. M. Niczyporuk,[e] L. Nodulman,[a] W. Orejudous,[g] T. J. Phillips,[b] K. T. Pitts,[c,e] W. Reigler,[d] R. Richards,[i] C. Rivetta,[c] W. J. Robertson,[b] R. Roser,[e,c] L. Sadler,[g] R. Sandberg,[c] S. Sansone,[d] R. Schmitt,[c] K. Schultz,[c] D. Shuman,[g] R. Silva,[c] P. Singh,[e] R. Snihur,[k] P. Tamburello,[b] J. Taylor,[g] R. Thurman-Keup,[a] D. Tousignant,[c] F. Ukegawa,[j] R. Van Berg,[j] G. Veramendi,[g] T. Vickey,[e] J. Wacker,[g] R. L. Wagner,[c] R. Weidenbach,[g] W. C. Wester III,[c] H. H. Williams,[j] P. Wilson,[c] P. Wittich,[j] A. Yagil,[c] I. Yu,[c] S. Yu,[j] J. C. Yun[c]

[a]*Argonne National Laboratory, Argonne, Illinois 60439 USA*

[b]*Duke University, Durham, North Carolina 27708 USA*

[c]*Fermi National Accelerator Laboratory, Batavia, Illinois 60510 USA*

[d]*Havard University, Cambridge, Massachusetts 02138 USA*

[e] *University of Illinois, Urbana, Illinois 61801USA*

[f]*The Johns Hopkins University, Baltimore, Maryland 21218 USA*

[g]*Ernest Orlando Lawrence Berkeley National Laboratory, Berkeley, California 94720*

[h]*University of Michigan, Ann Arbor, Michigan 48109 USA*

[i]*Michigan State University, East Lansing, Michigan 48824 USA*

[J]*University of Pennsylvania, Philadelphia, Pennsylvania 19104 USA*

[K]*University College London, London WC1E6BT, United Kingdom*

Elsevier use only: Received date here; revised date here; accepted date here

---

Abstract

The Central Outer Tracker is a large cylindrical drift chamber constructed to replace CDF's original central drift chamber for the higher luminosity expected for Run 2 at the Fermilab Tevatron. The chamber's drift properties are described in the context of meeting the operating requirements for Run 2. The design and construction of the chamber, the front-end readout

electronics, and the high voltage system are described in detail. Wire aging considerations are also discussed.

PACS-1996: 29.40.-n; 29.40.Cs; 29.40.Gx; KEYWORDS: CDF; Central; Outer; Tracker; Drift; Chamber;

1. Overview

The Collider Detector at Fermilab (CDF) required major upgrades to cope with the higher instantaneous luminosity and shorter bunch crossing times of the Fermilab Tevatron in Run 2. In earlier runs, the Tevatron operated with 6 bunches and a minimum of 3500 ns between bunch crossings. Initially in Run 2, the Tevatron is operating with 36 bunches and a minimum of 396 ns between bunch crossings.

When the instantaneous luminosity approaches 2×10^{32} $cm^{-2}s^{-1}$ and the number of interactions per crossing reaches ~5, the original Run 2 scenario had the Tevatron converting to 108 bunch operation with a minimum of 132 ns between crossings. While this is still an option, the present plan is to stay with 36 bunches and implement luminosity leveling if the luminosity exceeds 2×10^{32} $cm^{-2}s^{-1}$. This paper describes an upgrade to the CDF central drift chamber that can operate well in either the 36 or 108 bunch mode.

In Run 2, as in previous runs, the charged particle tracking at large radii in the central pseudo-rapidity region ($|\eta| < 1$) is done with a large open cell, cylindrical drift chamber using a readout that can record multiple hits from each sense wire. The goal of the Central Outer Tracker (COT) is to reproduce the positive characteristics of the Run 1 Central Tracking Chamber (CTC) [1] in the Run 2 environment, improve upon its capabilities where possible, and fit into an integrated CDF tracking plan.

Figure 1 is a side view of the central CDF detector, upgraded for Run 2 [2]. The COT [3] is located within a 14.1 kG solenoidal magnetic field, in the radial region outside the silicon microstrip detectors and inside the time-of-flight (TOF) scintillators. The active volume of the COT spans 310 cm [122 inches (in.)] in the beam (axial) direction, z; between 43.4 cm (17.1 in.) and 132.3 cm (52.1 in.) in radius, r; and the entire azimuth, ϕ.

The COT contains 30,240 sense wires that run the length (in z) of the chamber between two end plates. Approximately half of the wires are axial (run along the z direction) and half are small angle (2°) stereo. A reconstructed track provides accurate information in the r-ϕ view for the measurement of transverse momentum, p_T, and substantially less accurate information in the r-z view for the measurement of η.

1.1. COT drift cell, comparison to CTC

The COT contains 96 sense wire layers in radius that are grouped into eight "superlayers", as inferred from the end plate section shown in figure 2. Each superlayer is divided in ϕ into "supercells", and each supercell has 12 sense wires and a maximum drift distance that is approximately the same for all superlayers. Therefore, the number of supercells in a given superlayer scales approximately with the radius of the superlayer.

The supercell layout, shown in figure 3 for superlayer 2, consists of a wire plane containing sense and potential (or field shaping) wires and a field (or cathode) sheet on either side. Both the sense and potential wires are 40 μm diameter gold plated tungsten. The field sheet is 6.35 μm (0.00025 in.) thick Mylar [4] with vapor-deposited gold on both sides. Each field sheet is shared with the neighboring supercell. The supercell is tilted by 35° with respect to the radial direction to compensate for the Lorentz angle of the drifting electrons in the magnetic field. Section 16.1 addresses the electrostatic and drift properties of the supercell.

Table 1 compares the basic features of the COT and the Run 1 CTC, which also used the superlayer - supercell design. The most important difference is that the spacing between CTC supercells (and thus the maximum drift distance) is larger by a factor of four. Table 2 summarizes the superlayer geometry of the COT, and table 3 lists the materials and their radiation lengths in the COT active volume.

1.2. Reasons for choosing the COT design

The reasons why a Run 2 upgrade was necessary and why the COT design was chosen are discussed below.

1.2.1. Resolve bunch crossings (minimize occupancy)

The simplest strategy for operating a wire chamber in Run 2 is to ensure that the maximum drift time is less than the 396 ns bunch spacing in 36 bunch operation and less than 132 ns in 108 bunch operation. A maximum drift time of about 100 ns is achieved in the COT, which has a maximum drift distance of 0.88 cm, when using a fast drift velocity gas mixture such as argon / ethane / CF_4 (50:35:15). A more standard gas like argon / ethane (50:50) can be used when running with 36 bunches. The maximum drift distance of the CTC was too large to resolve bunch crossings in Run 2, so the CTC would have suffered significantly from event pileup and had to be replaced.

1.2.2. Retain proven features of CTC design

The CTC superlayer / supercell design provided a robust tracker up to the maximum Run 1 instantaneous luminosity of 2×10^{31} $cm^{-2}s^{-1}$. The increase in the number of bunches, the shorter drift space, and significantly faster readout combine so that the COT in Run 2 will see similar occupancies at 1.6×10^{32} $cm^{-2}s^{-1}$ in 36 bunch operation and at 4×10^{32} $cm^{-2}s^{-1}$ in 108 bunch operation. We can infer that the COT will be a robust tracker at these operating points, which is a good match for the expected instantaneous luminosities in Run 2.

1.2.3. Improve stereo superlayers

CTC tracking inefficiencies at high instantaneous luminosity mainly occurred due to the lack of unambiguous stereo hits from supercells that contained only 6 sense wires (see table 1). The COT has 12 sense wires in the stereo supercells, which should lead to better pattern recognition and tracking efficiency in busy events.

1.2.4. Field sheet versus field wire plane

The CTC used wires to form the field (or cathode) plane in its supercell. The field sheet in the COT allows for operation at significantly higher electric fields, which is necessary for Run 2 operation (see table 1). In comparison to wires, the sheet also provides more uniform drift trajectories near the cell boundary and introduces less material into the tracking volume.

1.3. Mechanical design

A photograph of the COT during construction is shown in figure 4. The basic structure creating the gas volume is a carbon / epoxy composite inner cylinder, a concentric aluminum outer cylinder, and annular aluminum end plates connecting them at both ends. For obvious reasons, this structure is referred to as the Can. Slots in the end plates, shown in figure 2, locate and support the wire planes and field sheets at the two ends. There is no additional support structure between the end plates. In an axial superlayer, the end boards of the wire planes and field sheets are installed into slots at the same ϕ at the two ends. A 2° stereo superlayer is achieved by stepping 12 slots (or 6 supercells) at one end relative to the other.

The wire planes and field sheets are installed with tensions that are sufficiently large and accurate to ensure accurate location and limited deflection due to gravitational and electrostatic forces throughout the active volume (see section 16 for details). The nominal wire plane tension is 4.350 kg (150 g × 29 wires as described below), the nominal field sheet tension is 9.988 kg, and the total load on the Can is 36132 kg [2520 supercells × (4.350 kg + 9.988 kg)].

The schedule for the CDF upgrade demanded that the wire planes and field sheets be ready for installation immediately after the Can was assembled, so they had to be manufactured at the same time as the Can components. An accurate finite element analysis of the Can under full load was required in order to predict the deflection of the end plates and thereby the corresponding lengths of the wire planes and field sheets. Sections 2, 3 and 4 will describe the components of the Can (including the finite element

analysis), the wire planes, and the field sheets, respectively.

2. The Can

2.1. End plates

The design of the COT calls for precisely machined end plates as shown in figure 2. Looking at these narrow slots, Electrical Discharge Machining (EDM) immediately comes to mind as the best machining technique. Unfortunately, no machining company had an EDM that could accommodate the radial span of the end plate, and we therefore chose to have the end plates machined with an end mill. Brenner Tool and Die, Inc [5] machined the end plates.

A more detailed drawing of the sense slot is shown in figure 5. The end plate is made of 6061-T651 aluminum and is 4.128 cm (1.625 in.) thick, which was the maximum value that machining companies said they could manage with the narrow slot width of 0.318 cm (0.125 in.).

In order to ensure that we had enough material for two good end plates, four pieces of aluminum stock, 3.05 m (120 in.) square by 5.72 cm (2.25 in.) thick, were purchased from Pierce Aluminum Company, Inc. [6]. Before machining started, several tests were performed on the stock plates. Each was thoroughly scanned for voids using ultrasound, and one was rejected. Cut-off sections were measured for yield strength [2.84×10^5 kPa (41.2 kpsi)], ultimate strength [3.11×10^5 kPa (45.1 kpsi)], and chemical composition (all elemental components were within acceptable range). On four occasions during the machining of each end plate, internal stresses were relieved using vibratory techniques. Approximately 33% of the end plate mass is removed by machining the slots.

The wire planes and field sheets are positioned by seating them to accurately machined features on the inside (drift gas side) of the slots. As shown in figure 5, within each slot the number of precision edges with tight tolerance is small: one surface of the slot for both the wire plane [± 50.8 μm (0.002 in.)] and field sheet [± 76.2 μm (0.003 in.)], and one edge of the "notch" for the wire plane [± 38.1 μm (0.0015 in.)]. The notch is only necessary for the wire plane, because while sense wires need to be precisely located along both the length (in plane) and width (orthogonal to the plane) of the supercell, only the precise location along the width is required for the field sheet. There are mating precision surfaces on the end boards of the wire planes and field sheets that are described in sections 3 and 4.

In addition to the slots, there are other machined features in the end plates, including:

- Twelve accurate [50.8 μm (0.002 in.) true position] survey holes around the outer diameter (OD), which were used to align the end plates during assembly of the Can and later to locate the completed chamber in the CDF detector.
- Shallow grooves between superlayers for mounting the "gas seal extrusions" (section 6.2).
- Steps on the inner diameter (ID) and OD for mating with the inner and outer cylinders.
- Numerous threaded holes for attaching the outer cylinder, attaching the fixture used to align the end plates during assembly of the Can, and attaching the fixture used to move the completed Can.

The locations of the precise portion of each slot surface and notch edge were measured with respect to the twelve survey holes using a Coordinate Measuring Machine with a measurement accuracy of ± 12.7 μm (0.0005 in.). The measurements were saved to use during the alignment of the two end plates and for geometry corrections in the off-line analysis. During assembly of the Can (section 2.4), the survey holes in the two end plates were aligned to produce the optimal match in ϕ for slots directly opposite each other (those used for the same wire plane or field sheet in axial layers).

2.2. Outer cylinder

Figure 6 includes an overhead view of the Can, which shows the outer cylinder attached to the end plates. The outer cylinder carries most of the load on the end plates (~22000 kg) and locks the two end plates into position after the alignment described in section 2.4. The outer cylinder was machined by STADCO [7].

The outer cylinder is not a single piece, but is divided into eight equal sections in ϕ. Each section consists of a "stave", "cover plate", and two "patch plates"; all made of 6061-T651 aluminum. Figure 7 is an enlargement of a region near the end plate. The stave is 20.32 cm (8.0 in.) wide (in ϕ). The thickness (in r) is 0.953 cm (0.375 in.) in the central region and tapers down to 0.635 cm (0.250 in.) to match that of the cover plate. The length (in z) is accurately machined to set the distance between the inside of the end plates.

The cover plate is 0.635 cm (0.250 in.) thick and spans the region between the staves [86.678 cm (34.125 in.) arc length]. Both the stave and cover plate are screwed into a shelf in the end plate perimeter. The depth (in r) of the shelf is just enough so that the outer cylinder, including screws, never extends beyond the perimeter of the end plate. The cover plate is left slightly undersized in length (z), and the gap is filled with Stycast 2850 epoxy [30], which has sufficient compressive strength to carry the load on its own.

The stave and cover plate are joined along their entire length by the overlapping patch plate. The patch plate is 0.635 cm (0.250 in.) thick and 8.95 cm (3.52 in.) wide and is screwed down to the stave and cover plate every 7.62 cm (3.0 in.) along the length.

As seen in figure 6, two rectangular holes were left in each cover plate in order to gain access to the interior of the Can during installation of the wire planes and field sheets. After the installation was complete, "hatch covers" were screwed into place.

All screws are 18-8 stainless steel and were installed dry. In order to complete the gas seal, 3M Scotch-Weld 2216 structural epoxy [8] was later used to fill the counter sink around each screw head and to create a fillet along the corners where two aluminum pieces overlap.

2.3. Inner cylinder

The inner cylinder is between the beam and the active area of the COT, so the material was kept to a minimum consistent with the requirement of carrying an ~14000 kg load. The main portion of the cylinder is a carbon fiber / epoxy composite with an average wall thickness of 0.251 cm (0.099 in.) and an average outer diameter of 81.161 cm (31.953 in.). It has aluminum end rings that contact a shim within a shelf in the COT end plate as shown in figure 8. Advanced Composites, Inc. [9] made the inner cylinder.

The main portion was filament wound on a mandrel using Toray T700 12K carbon fiber [10], and Dow 383 Epoxy [11] (with Air Products Ancamine 2167 curing agent [12]). It has a total of six layers: three hoop layers wound at 90° with respect to the axis and three helical layers wound at ± 25° with respect to the axis. The 6061-T6 aluminum end rings were attached to the composite cylinder using Hysol EA9430 adhesive [13].

As shown in figure 8, silver epoxy was placed between the machined end of the main portion (r-ϕ surface) and the aluminum end ring in order to provide good electrical connection between the ends of the carbon fibers and the end plate. A 25.4 μm (0.001 in.) thick aluminum sheet was epoxied to the outside of the cylinder (side facing the COT gas volume) to provide both additional electrical shielding and isolation of the cylinder from the gas volume. The sheet was attached to the end rings using silver epoxy. The electrical shielding has proved adequate, since there has been no evidence of pick-up from either the accelerator or silicon detector when taking collision data. At normal incidence, we estimate that the material in the main portion of the cylinder corresponds to 0.99% of a radiation length.

The inner cylinder was tested at a factor of 1.5 above the nominal axial load using a hydraulic press. The cylinder compressed by 0.112 cm (0.044 in.) at 13620 kg (30000 lb), which is close to the nominal load. The factor of safety against buckling, defined as the nominal load versus analytic buckling point for a perfect cylinder, is eight.

As shown in figure 8, the inner cylinder is held to the shim and end plate only by friction due to the load (no epoxy or screws). This allowed the end of the cylinder to pivot on its edge when the load was applied and the end plate deflected, thereby minimizing the stress on the epoxy joint between the main composite section and the aluminum end ring. The ~0.381 cm (0.150 in.) thick shim ring was machined shortly before assembly of the Can and compensated for variations in the "as built" parts from nominal and for the initially unknown compression of the cylinder under load. The shim on the East side varied in thickness by 0.023 cm (0.009

in.) as a function of ϕ to compensate for variation in the depth of the shelf in the end plate.

2.4. Alignment and assembly of the Can

Each aluminum end plate weighs ~409 kg (900 lb), so the fixture used to align the end plates and assemble the Can was necessarily massive to minimize deflections. The Can was assembled with its axis vertical. The end plates were held near the top and bottom of a 396 cm (156 in.) high × 335 cm (132 in.) × 335 cm (132 in.) steel frame called the Alignment Fixture, which is shown along with the partially assembled Can in the photograph in figure 9. The fixture was machined and assembled by STADCO. During the alignment and assembly of the Can, the Alignment Fixture was located in a clean room with accurate temperature control, so that the temperature of the Can was within ± 1° F of the nominal 69° F.

Differential struts, with spherical bearings on both rod ends, joined each end plate to the steel frame at eight equally spaced locations around the perimeter. Both the top and bottom end plates had a strut with vertical adjustment at each of the eight attachment points in order to level each plate and adjust the distance between the plates. Only the top end plate had additional struts in the horizontal plane to adjust its relative translation and rotation with respect to the bottom. The breakaway force of the spherical bearings in the rod ends was on the order of 4.5 to 6.9 kg (10 to 15 lb), which was large enough to prohibit incidental motion, but small enough to move easily with the plate when adjusting the struts. After the adjustments were made, the plate was locked into place with a clamping system that bypassed the struts.

The following procedure was used to assemble and align the Can. The bottom end plate was attached to the Alignment Fixture, the inner cylinder was set into the step in the ID of the bottom end plate, and the top end plate was attached to the Alignment Fixture, trapping the inner cylinder. The end plates were leveled and roughly aligned in relative distance, translation and rotation, so that they were well within the adjustment range of the differential struts.

The staves were screwed into place at eight locations between the vertical struts, fixing the distance between the inside (gas side) surface of the end plates at those points. The vertical struts were then adjusted to give the same average distance at their locations using a stick micrometer. The staves are narrow in ϕ, so they did not inhibit further adjustments in translation and rotation.

The 12 accurate survey holes (50.8 μm true position) around the OD of each end plate were targeted to align the end plates in translation and rotation. Since the plates were both level, an optical transit was used to align matching survey holes (a nearby plumb line defined the vertical sweep of the transit). Light reflected from precisely round ball bearings set into the inside surface of the survey holes provided the actual targeting for the transit. The survey holes were aligned to a "best fit" value to an accuracy of ±25.4 μm (0.001 in.). The rotational alignment was independently checked using a Hamar laser system.

"Pre-string" lines were run between appropriate end plate slots (these lines were later used to pull the wire planes and field sheets into the chamber). With the pre-string lines in place and the alignment complete, the remaining outer cylinder pieces, the cover plates and patch plates, were screwed into place. In order to verify that the alignment was now locked in, the relative positions of the survey holes were monitored when the top end plate was released from the Alignment Fixture, and the end plates remained in rotational alignment to within the ±25.4 μm (0.001 in.) accuracy of the measurement.

2.5. Finite element analysis of Can under full load

Finite element analysis (FEA) was used to predict the deflection of the end plate under the 36132 kg load of the wire planes and field sheets. The result is shown in figure 10, along with measurements made after the Can was assembled and pre-tensioned (section 5.1). Due to the relatively thin wall between adjacent slots in the end plate, it was important to include shear, as well as bending, deformation in the model. The end plate support is simple at the ID (inner cylinder) and closer to simple than fixed on the OD (outer cylinder). The FEA

found a maximum stress point in the end plate of ~1.0×10^5 kPa (15 kpsi), compared to the measured yield strength of 2.84×10^5 kPa (41.2 kpsi).

The predicted maximum deflection of 0.538 cm (0.212 in.) is not negligible compared to the nominal stretch of the wire planes, 0.86 cm (0.34 in.), and field sheets, 1.02 cm (0.40 in.). Therefore, the manufactured lengths of the wire planes and field sheets are unique for each of the eight superlayers. The precisely machined portion of the slot on the gas side of the end plate was made 0.762 cm (0.300 in.) deep (see figure 5), which accommodated uncertainties in the FEA prediction and tolerances in the manufacture of the end plates, wire planes and field sheets.

Before assembling the Can, the deflection of the machined end plate at close to full load was measured using vacuum to simulate the force due to the wire planes and field sheets. The slots were covered and the plates were simply supported on the ID and OD at locations near those of the inner and outer cylinders. The measured deflection was within 15% of the FEA prediction.

3. Wire planes

Figure 11 is an isometric drawing of a wire plane, showing the wires, end boards and center support. Figure 12 shows the wire plane end board seated in an end plate slot. All wires - sense, potential, and shaper - are 40 μm diameter gold plated tungsten manufactured by Osram Sylvania [14]. The gold plating is 4 to 6% by weight (~ 0.92 μm thick), and there is a nickel strike of about 0.5% by weight beneath the gold. The wires were specified to have a minimum tensile strength of 2.76×10^6 kPa (400 kpsi), which is a factor of 2.4 over the nominal stress on a wire when strung at 150 g.

As shown in figure 3, each sense wire has a potential wire on either side to form the drift cell, and the nominal spacing between sense and potential wires is 0.3556 cm (0.140 in.). At each end of the plane of wires is an additional pair of shaper wires, which operate at the same voltage as the end potential wire and shape the drift trajectories at the end of the supercell. The spacing between the end potential wire and the first shaper wire is 0.3556 cm (0.140 in.), and the spacing between the shaper wires is 0.1778 cm (0.070 in.). The center support is a 0.1588 cm (0.0625 in.) diameter polyester / fiber glass "pultrusion" rod that is epoxied to each wire in the plane to limit the stepping of wires out of the plane due to electrostatic forces (see section 16.2). The mass of the rod is ~12 mg.

3.1. Wire plane end board, wedge, insulation

The wire plane end board has several components: the G10 printed circuit (PC) board, the 50.8 μm (0.020 in.) diameter gold plated copper pins, the shim made of liquid crystal polymer (LCP), the LCP pin cover, and the G10 ledge. As shown in figure 12, the wires are epoxied to the end of the PC board on the gas side and soldered to 0.0508 cm (0.020 in.) wide pads. Traces from these pads lead to pads on the other end of the board where the pins are soldered. "Motherboards" plug into the pins to connect the wires to high voltage on one end plate and to the readout on the other (see section 6.1).

As shown in figures 12 and 13, the shim is epoxied to the end of the PC board on the gas side and has precise features, the ridge and nib, which mate with the precise slot edge and notch edge, respectively. The pin cover insulates the pins from the end plate and transfers the 4.350 kg load of the wire plane through the ledge to the end plate.

The PC board was made from 50.8 μm (0.020 in.) thick copper-clad G10 CR. The CR (cryogenic) grade was used to avoid the out-gassing of flame retardant in G10 FR4. The shim and pin cover were injected-molded using Vectra A130 glass reinforced LCP [15]. As seen in figure 13, these parts required some long features with small cross section, and this LCP was both able to flow well in the mold and have sufficient strength for later handling. A precise fixture was used to position the shim and pin cover when epoxying them to the PC board. Another precise fixture was used to align the pins when soldering them to the PC board.

The G10 wedge is the other part shown inside the slot with the end board in figure 12. It is a spring that pushes between the slot and two lines on the end board, forcing the precise shim against the precise slot surface on the gas side and forcing a "back shim" against the slot on the atmosphere side. The back

shim is a slight protrusion on the pin cover for the wire plane and simply a wire epoxied on the end board for the field sheet. The shims are large enough so that the end board proper will not contact the less accurately machined part of the slot and thereby interfere with the seating of the precise shim. This is also the reason why the back shim is placed as far as practical from the precise shim.

Since the sense and potential wires operate at high voltage, the wires and the traces and connectors on the end board must be isolated from the end plate. The pin cover shields the pins and associated solder pads and traces on the atmosphere side of the slot. Most of the trace length and the wire solder pad are on the same side of the end board as the wedge, so the wedge is made insulating to shield them from the slot (and itself). Note that the field sheet wedge need not be insulating, but it is the same design. As the sense or potential wire leaves the epoxy strip and enters the active volume, it is shielded from the slot by the precise shim on one side and by a Kapton sheet on the other. The Kapton sheet is epoxied to the side of the wedge away from the end board.

3.2. Assembling the wire planes

A critical part of the COT assembly was to accurately relate the position of the wires to the precise edges on the end plate slot and notch. This was accomplished by

1) Accurately relating the position of the wires to the ridge and nib on the shim during the wire plane assembly.
2) Snugly seating the ridge and nib to the mating end plate features during plane installation into the Can.

The first step was accomplished using a grooved rod to accurately position the wires with respect to a reproduction of the end plate's precise edges (to which the end board was seated) during the wire plane assembly.

A screw manufacturer machined stainless steel grooved rods, called combs, cheaply and with excellent accuracy. Both the position along the rod and the depth of the triangular groove was specified to be within 12.7 μm (0.0005 in.) of true position, and this was verified by measuring each comb on a shadowgraph.

A winding machine was used to assemble 22 wire planes simultaneously. Eleven planes were set up on a transfer frame, and a transfer frame was mounted to both sides of the rotating portion of the machine. The equivalent to the slot edges and notch edges in the end plate were mounted along both ends of the transfer frame, and the combs were positioned with respect to these features using gauge blocks. The position and speed of the wire feeder on the winding machine were adjusted so that the wire would fall within the wide part of the groove on the outer diameter of the comb, and the 150 g winding tension forced the wire to the bottom of the groove. The tensions within a wire plane were distributed with a typical standard deviation of 1.1 g.

We needed to allow for the change of length of the wire planes from superlayer to superlayer and also allow for the center support to be epoxied to the wires without disturbing the wire position. Both were accomplished by mounting pairs of combs above the nominal plane of the transfer frame by an amount that increased commensurate with the required increase in length of the wire plane. The combs were located on either side of center, so that the wire positions were locally fixed.

The following steps were performed to make a new set of 22 wire planes:

- Inspect and clean the fixtures on the two transfer frames, including the precise slot edges, notch edges, and combs and mount the transfer frames on the winding machine.
- Adjust the height of the center comb fixture for the particular superlayer.
- Scotch-brite [8] the copper pads on the PC boards (for soldering) and clean the end boards with alcohol.
- Seat the end boards against the slot and notch edges and clamp them down.
- Load a new 5 km spool of wire on the winding machine feeder and wind over the 22 planes. Check that all wires fall into the appropriate comb grooves.
- Apply a temporary epoxy bead on the edge of the transfer frame beyond the end boards. After the epoxy is cured, cut the wires between the two frames, so that each frame can be removed from the winding machine.

- The wires have a small clearance above the surface of the end board, so that their position is determined by the grooves in the comb.
- Apply a controlled Epolite 5313 epoxy [16] bead over the wires on the gas side edge of the end board (near the comb). A strip of Mylar is placed over the bead to control the spread along the board.
- After the Epolite 5313 is cured, solder the wires to the pads and epoxy the center support. Either the Epolite or the solder connection alone is adequate to hold the wire tension.
- Trim the wires at the back of the solder pads, inspect, and add necessary insulation to the shaper wires (Kapton [4] pieces and Corona Dope [17]).

The wire planes are then removed from the transfer frame and placed under slight tension in a storage box. Epolite 5313 was chosen to secure the wires because it is very hard and does not allow transverse creep of the wire through the epoxy in the case of the stereo layers.

3.3. Measurements of the wire planes before installation

The wire planes went through a number of tests before installation into the Can. One set of measurements was made as soon as possible after assembly, so that we could monitor quality:

- Tension of each wire when the plane is stretched to nominal length.
- Operation at high voltage in a simulated supercell with Sr^{90} sources that produce radiation levels similar to those that will be seen in Run 2.

The tension measurements were performed on all wire planes. Due to time and equipment constraints, only 57% of the planes were tested under high voltage with the sources.

The tension measurement was made using a PC running Lab Windows [18]. The planes were placed in a magnetic field and each sense and potential wire was driven with a sinusoidal varying voltage through the resonant frequency. A lock-in amplifier measured the out-of-phase component, which went to zero at resonance and then changed sign. As noted earlier, the typical standard deviation of tensions within a plane was measured to be 1.1g. In addition to 16 planes with connection problems that were subsequently corrected, 2 planes were rejected for greater than 5% variation in tension across the plane, and 9 planes were rejected for having one or more wires with tension greater than 4 g from the plane average.

The high voltage test was made with the wire plane inside a simulated supercell using a drift gas of argon / ethane (50:50) and ~1% isopropyl alcohol. It consisted of monitoring current draw from the power supplies while an Sr^{90} source was stepped slowly along the length of the plane during a 9-hour period. The wire currents varied from ~11 nA/cm for wires at the edge to ~140 nA/cm for those near the center. This approximately corresponds to wire currents in SL1 at instantaneous luminosities of 10^{32} $cm^{-2}s^{-1}$ and 10^{33} $cm^{-2}s^{-1}$, respectively. Rejected planes included three with excessive currents without sources, four with increased currents with sources due to possible glow, and five due to failure to hold high voltage during the course of the test. A significant fraction of these failures were believed to be due to measurement problems, but the planes were rejected in any case.

Another set of measurements were performed at a later time:

- Measure the length of the plane at nominal load.
- Measure the position of the wire in plane to an accuracy of ~7.62μm (0.0003 in.).
- Go / no-go test on the wire position perpendicular to the plane [less than 76.2μm (0.003 in.)].
- Check for continuity between the pins on one end board to the appropriate pins on the other.

All wire planes were subjected to the four tests. The tests were performed on a fixture with a precise slot edge and notch edge on each end to which the end boards were seated and clamped.

On one end only, the end board mount was attached to a very low friction slide, and the length was measured when the load was applied. As explained in section 5.3, this length measurement was used in conjunction with the measured distance between the outside surfaces of the end plates (after pre-tensioning) in order to determine the width of the G10 ledge, which was attached to the end board just before the plane was installed into the Can. The ledge provided a fine tuning of the wire tension,

correcting for variations in the wire plane manufacture and for differences between the actual distance (in z) between end plate slots and that predicted by the finite element analysis.

On the "fixed end" of the fixture, a PC optical scanner was placed just beneath the wire plane near the end board. The scanner measured the in-plane wire position to an accuracy (rms) of 7.62μm (0.0003 in.). The standard deviation of the difference between the actual and nominal wire positions is 13.2 μm (0.00052 in.). Planes were rejected if any sense wire position was more than 76.2 μm (0.003 in.) from nominal or any potential or shaper wire position was more than 127 μm (0.005 in.) from nominal. About 5% of the planes were rejected. The measured in-plane wire positions were saved for later geometry corrections in the off-line analysis.

4. Field sheets

Figure 14 is an isometric drawing of a field sheet, including the gold / Mylar sheet, the 305 μm (0.012 in.) diameter stainless steel edge wires, the aluminum end boards, and the glass tube center support. The sheet has 350 angstroms of gold vapor deposited to both sides of the 6.35 μm (0.00025 in.) Mylar material. Gold was chosen because of its good conductivity, high work function, resistance to etching by positive ions, and low chemical reactivity. Sheldahl Corporation [19] manufactured the material in roll form.

Approximately 90% of the load is carried by the stainless steel (316 alloy) edge wires, which are epoxied to the sheet along their entire length. The wire has a tensile strength of 1.55×10^6 kPa (225 kpsi) and was manufactured by Major Wire Co. [20] in 365.8 cm (144 in.) straight lengths. The wires are attached in a parabolic shape [sagitta = 1.02 cm (0.40 in.)] in order to maintain transverse force on the sheet to control sag and ripples. Both the wires and the gold / Mylar sheet are epoxied to the end boards.

As discussed in more detail in section 16.2, the deflection of the sense wires due to electrostatic forces is substantially reduced at large drift field by the addition of a center support on the field sheet. The center support is a borosilicate glass capillary tube with 1.2 mm outer radius and 0.69 mm inner radius. It is epoxied to the field sheet and completely covered by a "flap" of the gold / Mylar material. The flap is epoxied to the field sheet, and is electrically connected to the sheet with silver epoxy at both ends. The purpose of the flap is to prevent charge up and possible glow from the epoxy attaching the rod to the sheet.

4.1. Field end board

The field sheet is operated at ground (end plate) potential, and an aluminum end board was used. Figure 12 shows the end board seated in the end plate slot. The main portion of the end board, shown in figure 15, was machined from 0.0787 cm (0.031 in.) thick 6061-T6 aluminum. The field shim, which mates with the precise surface of the end plate slot, was machined from 2024-T351 aluminum and epoxied to the main portion using a precise fixture.

The relationship of the gold / Mylar sheet, wires, main end board and shim is best seen in the end view in figure 15. The design is complicated by the arc on the gas side of the end board, which was found to significantly reduce rippling compared to the case where the sheet was epoxied to an end board with a straight edge. It was critical to maintain an accurate relationship between the precise edge of the shim and both the wires and the sheet.

The stainless steel wire was epoxied into a 0.0381 cm (0.015 in.) deep by 0.0483 cm (0.019 in.) wide groove that runs the entire 5.398 cm (2.125 in.) length of the end board. In order to prevent the wire from possibly creeping transversely out of the groove (most important for the stereo layers), a 127 μm (0.005 in.) thick 5052-H19 aluminum cover was epoxied over the grooves. The cover actually extended over most of the end board surface in order to prevent damage of the gold / Mylar material during installation into the end plate slot.

Because they were attached with a normal (electrically insulating) epoxy, electrical contact between the stainless steel wires, the gold / Mylar and the end board is not guaranteed. A brass grounding clip, spanning the board edge, was attached with silver epoxy, making positive contact to the wire, gold (both sides of sheet) and the bare aluminum side of the end board. The stainless steel wires were left long and bent around the edge of

board before epoxying the clips, so this also serves as a mechanical back up to the epoxy joint in the groove.

The aluminum ledge, shown in figure 15, transfers the load of the sheet to the end plate. Flat head screws pass through precisely located counter sunk holes in the end board and screw into tapped holes in the ledge. Excellent electrical contact is made when the edge of the ledge seats against the end plate surface with the 9.99 kg (22 lb) load. As with the wire plane, the field sheet ledge is machined to its final dimension shortly before installing the sheet into the Can in order to compensate for the difference in the field sheet's manufactured length from nominal and the difference between the actual and calculated deflection of the end plate.

4.2. Assembling the Field sheet

Attaching the wires to the sheet and both the wires and sheet to the end boards was done at the same time using a pallet with precise fixtures to locate and hold the end boards and to guide the wires. Figure 16 is a sketch of the pallet that greatly exaggerates the curvatures of the wire guides and base. Figure 17 is a photograph of one of thirty pallets (base, wire guides and end card holder), a roll of gold / Mylar, and a fixture for applying the epoxy. The pallet surface and the edges of the wire guides were covered with Teflon film [4] to prevent epoxy from sticking to the fixture itself.

The following steps were performed during the first stage of assembly:

- Set the field sheet length for the superlayer by adjusting the position of the end board holding fixture relative to the end of the wire guide.
- Spray the pallet surface with ethyl alcohol, unroll the 15.24 cm (6 in.) wide gold / Mylar sheet over the pallet, and smooth it wrinkle free to the pallet surface using a rubber squeegee.
- Clamp down the wire guides over the sheet and place the stainless steel wires along them. The wires are held at small tension [~0.341 kg (0.75 lb)].
- Start the motor for the epoxy applicator. The epoxy is applied through syringes with flexible tips that ride along the joint between the wire and sheet. A typical pressure for applying the epoxy was 207 kPa (30 psi). The epoxy contains Epon 828 resin [21] (63% by weight), Air Products Ancamide 506 curing agent [12] (35%) and Cab-O-Sil glass bead filler [22] (2%). The Cab-O-Sil controls capillary flow under the edge of the wire guide.
- Fill the grooves and coat the surface of the end boards with the same epoxy mixture without Cab-O-Sil .
- Insert the end board into the end board holder and the stainless steel wires into the grooves. Clamp the holder, pressing the end board to the sheet.
- For stereo layers, the end boards are rotated by an angle of 1.13° in order to have equal forces on the stainless steel wires without having to allow for this angle within the end plate slot.
- Place the pallet in a curing rack overnight. At least several hours after the epoxy is applied, turn on heat lamps to ensure a reasonable cure by the next day. One could typically produce 12 to 16 sheets per day.
- The next day, trim the excess gold / Mylar material from the edges of the sheet. In the longitudinal center, the sheet extends beyond the wire by ~0.635 cm (0.25 in.). This "wing" is necessary to control drift trajectories at the ends of the supercell and electrostatic deflections. Careful inspection ensures that epoxy has not wicked appreciably into the wing area.
- Place the field sheets under small tension in a storage box (~30 sheets per box). They move in and out of the storage box during the next stages of assembly and testing.

After the epoxy was fully cured, the sheet was tested at full load for length and shape. Since Mylar expands when it absorbs water, the length measurement was corrected for the relative humidity (RH) in the clean room [~3.8 μm (0.00015 in.) / %RH]. The standard deviation of the measured lengths was ~127 μm (0.005 in.), and a sheet was rejected if the length was greater than 381 μm (0.015 in.) from nominal. Less than 1% of the sheets were rejected due to the length requirement.

The shape measurement demanded that the sheet lie within a ±127 μm (0.005 in.) window of nominal. Only a few sheets had overall shapes outside tolerance, but ~10% were rejected due to local ripples

with amplitudes greater than 254 μm (0.010 in.). Most of the rippling was due to problems inherent with the gold / Mylar material.

More assembly and tests were required for sheets that passed the length and shape tests. The aluminum end board cover, the brass grounding clips, and the center support still had to be attached. In addition, we found that the epoxy attachment between the shim and end board was too delicate for eventual installation of the sheet into the Can, so a larger bead was applied which had the side effect of directly attaching the shim to the gold / Mylar sheet.

Both the center support attachment and shim epoxy reinforcement had to be done at the full 9.99 kg (22 lb) load. In order to save time and minimize handling, the attachment of the end board cover was incorporated into the same fixture.

Ten parallel fixtures were used to tension 10 sheets and do the above operations simultaneously. The epoxy was cured at elevated temperature (~140° F) starting just after application, so that the sheets could be removed from the fixtures after about 1 hour of curing time. The silver epoxy connections at the brass grounding clips and the center support flap were made just before the sheets were placed back into their storage box. Approximately 50 to 60 sheets were processed each day.

After the epoxy was fully cured, the sheet was placed in a fixture to verify that its average mechanical properties were within tolerance. The fixture was basically a supercell with simulated wire planes defining the boundaries. The field sheet was placed into the center of the cell and stretched to the length previously measured under nominal load.

The capacitance was measured between the field sheet and each wire plane separately, and the difference indicated the average position of the sheet within the cell. This measurement was made at two orientations of the field sheet: horizontal with the stainless steel wires above the sheet and horizontal with the wires below the sheet. The gravitational sag of the sheet is significantly different in these two orientations. The measured average positions were required to be within ±76.2 μm (0.003 in.) of nominal, and only sheets with either broken or previously broken and poorly repaired shims failed this test. The sheets were used after the shims were repaired.

5. Wire plane and field sheet installation

Let us briefly recap the status to this point. The Can is aligned and assembled and the top end plate is released from the Alignment Fixture. The wire planes and field sheets are assembled and tested and reside in storage boxes under slight tension. There is a database with the measured lengths of each wire plane and field sheet at nominal tension.

The Can was then lifted out of the Alignment Fixture and rotated so that its axis was horizontal for wire plane and field sheet installation. In order to facilitate the installation, the chamber was set onto the four steel wheels (two wheels at each end plate) of the "rotation fixture", in which the ϕ orientation of the COT could be precisely adjusted. Part of the frame and one of the steel wheels of the rotation fixture can be seen in the bottom right hand corner of figure 4. A PC was used to control a Slo-Syn SS2540B synchronous stepping motor [23], which drove one of the wheels. One could reproducibly rotate and align to any slot on the end plate to an accuracy of 0.012 cm (0.005 in.).

5.1. Pre-tension fixtures, measure distance between pre-tensioned end plates.

Since the end plates would substantially deflect due to the load of the wire planes and field sheets, they were pre-tensioned using the fixtures shown in figure 18. A pre-tension fixture was installed into every fourth supercell. Both ends of a 660 μm (0.026 in.) diameter steel music wire were fed through the chamber using a pre-string line and were attached to a steel extension spring (Lee spring 135J-3 [24]) and a commercial right side guitar treble tuner mounted to the opposite end plate. The wire looped around a pulley (Sava LP22-UP48 [25]) on the original end plate.

The guitar tuner handle was turned, elongating the spring until the correct tension was achieved on the piano wire [28.7 kg (63.2 lbs)]. The required extension of each spring was calibrated to ~1% accuracy using a dead weight before mounting the fixture. Three iterations were required before the plates reached their final deflection.

With the end plates fully tensioned, nine dial indicators were mounted along the radial span of each

end plate at the same ϕ location to measure the distance between the outside surfaces. The dial indicators were zeroed on a flat granite table before mounting. The dial indicator readings were recorded every 15° in ϕ, the distance between the end plates at the ID and OD were measured with a stick micrometer at the same locations, and the measurements were combined to give the distance between the outside surfaces of the end plates at the nine radial and 24 ϕ locations. A fitting program was used to interpolate between measurements to produce a database with a distance for every slot location. Figure 10 shows that the actual deflection of the end plates agrees well with the FEA prediction if the prediction is increased by a factor of 1.19.

5.2. Plane installation fixture

The two sets of plane installation fixtures are shown in position in the clean room in figure 6. Each set consists of a near end fixture and a far end fixture. One set of fixtures was used to install wire planes and the other set field sheets.

The purpose of the installation fixture was to pull the plane through the chamber with controlled speed and tension and finally apply additional tension to "latch" the end board ledge to the end plate. While the plane was moving through the chamber, a load cell on the far engine monitored the tension. The far engine would cease pulling if the tension exceeded a safe value. The "stringing" tension of ~2.27 kg (5 lb) was set by a constant tension spring mounted on the near engine.

The installation process began by unrolling Dacron [4] strings from the spools of the near and far engines, attaching them to a pre-string end card, and pulling the pre-string completely out of the chamber on the near side. The pre-string was replaced with either a wire plane or field sheet, and the plane was pulled through the chamber and latched.

A curved G10 spring, called the wedge, was compressed between the end board and the side of the slot to prevent the wire plane or field sheet from moving, as shown in figure 12. The wedge only pressed the end board to the slot at the shim on the precise inside edge and at a coarse shim near the outside edge. The entire installation process typically took about five minutes.

We found it most convenient to install planes with end plate slots in a horizontal orientation, which occurred at roughly 4:00 and 10:00 when looking from the near end (see figure 4). After rotating the Can to the correct ϕ orientation using the stepping motor, the stringing engines were set to the appropriate x and y coordinates using the screw drives and rails. For stereo layers, the ϕ angles of the engines were also set.

Final adjustments to the engine alignments were made when pulling out the pre-string upon installing the first plane in a superlayer. The installation of subsequent planes in the superlayer required only the automatic indexing of the Can to the next slot location using the stepping motor.

5.3. Procedure used to string the chamber.

Due to the necessary realignment of the engines when changing superlayers, all wire planes and field sheets were installed in a superlayer before proceeding to the next one. Because the hatches in the outer cylinder allowed us some ability to recover from stringing problems inside the Can, we started stringing the inner superlayers and worked our way out.

The stringing had to minimally impact the end plate pre-tension and allow for the fact that the wire planes were considerably more delicate objects than the field sheets. Installing planes in groups of eight supercells satisfied these conditions:

- At the low (4:00) engine, remove the necessary pre-tension lines and install all the field planes in the group.
- Rotate the Can ~180° and install the wire planes between the field sheets using the high (10:00) engine. At the same time, install field planes in the new section of eight supercells at the low engine.
- Repeat the procedure until the superlayer is full.

Ledge machining and attachment were done at least a day before the plane was installed, since epoxy with a 24 hour cure was involved with the ledge attachment. The databases of the wire plane length at nominal tension, the field sheet length at nominal tension, and the chamber length at each slot were used to calculate the ledge widths. Both the wire plane and field sheet ledges were machined to their

required width using a router. The wire plane ledge, shown in figure 11, was attached to the end board pin cover using Epon 828 epoxy resin and Air Products Ancamide 506 curing agent. The field plane ledge, shown in figure 14, was attached to its aluminum end board using screws, and then the screws were potted with the same epoxy.

The wire plane ledge contacts the end plate in two distinct spots. This avoids the ambiguity of where a ledge with a straight surface would actually make contact. The field sheet ledge contacts the end plate at only one point, so the sheet can naturally equalize the tension on the two stainless steel wires (see discussion of the stereo sheet distortion in section 16.3).

During the day and evening shifts, wire planes and field sheets were installed in ~60 supercells and ledges were attached on the wire planes and field sheets to be installed on the following day. The night shift was reserved for the initial "seating" of the wire plane nib to the notch edge and quality control.

5.4. Quality control during stringing

During the owl shift, the tension of every wire in every wire plane installed during the previous day was measured. The wire tension was calculated from the measured frequency of resonance induced in the wire by driving it with an oscillating current at the resonant frequency in a magnetic field. The magnetic field was generated by permanent magnets placed along the ID and OD of the Can. Because of the center support on the wire plane, the resonant frequency of each half was determined by centering the magnets on the two halves for separate measurements.

A National Instruments [26] PCI E series ADC - DAC - I/O board was used with their Lab View program to perform the measurements. The program stepped through the wires in a plane, driving each wire with a current of known frequency. The wire connection was then switched from the driving current to an ADC input, and the amplitude of the induced current from the wire vibration in the magnetic field was measured. The frequency of the driving current was varied and the maximum induced amplitude indicated the resonant frequency. In order to keep up with the day's stringing, the "stepping algorithms" had to be optimized to measure all wires in a half-plane in a few minutes time. By feeding in the measured wire density and the length of the plane for that superlayer, the tension measurement was made to an accuracy of ~1%.

Planes were removed if any wire fell outside a ± 5% window around the nominal 150 g. Normally failures were due to the tension of the entire plane being shifted, and the plane could be re-installed after adjusting the size of the ledge.

The field sheet tension was not so easily measured, so only a small sample of the sheets were monitored on a daily basis by noting the load required to pull the ledge slightly back from the end plate. The field sheets were actually strung at a slightly higher than nominal tension (purposely overstretched by 635 μm (0.025 in.)) because there was some stress relaxation for the first few weeks after applying the load. Roughly six months after installation, the tensions of a sample of 10 sheets were measured to be the expected 9.99 kg (22 lb.) within the measurement error of ± 0.14 kg (0.3 lb).

5.5. Quality control and end board seating after stringing.

Soon after all field sheets and wire planes were installed, the tensions of all wires in the wire planes were re-measured and the same cuts were applied. At this point it was time to do the final seating of the wire planes and field sheets and then fix them in place for the long term by epoxying the end boards directly to the end plate.

The wire plane seating was particularly problematic. We examined all of the nibs and discovered that a few percent were damaged in the initial seating. The damage was correlated with notch edges that were rounded well beyond specification. For these cases, the wire plane end board was seated using a fixture that located the opposite, undamaged, side of the nib to the notch beyond the rounded edge. The width of the injection-molded nib was accurate to better than 0.0025 cm (0.001 in.), so this procedure did not introduce a significant loss in accuracy. After the end boards were all re-seated in a superlayer, their position was checked using a transit and a handful of mistakes

were corrected. At this point the end boards were epoxied directly to the end plate.

The field sheet had a different problem with seating. The position along the length of the slot was not critical and was easily set with a simple fixture. As discussed in section 16.3, for stereo layers it is necessary to have equal tension on the stainless steel wires, so that the sag of the plane and electrostatic forces are under control. In order to accomplish this, the ledge was momentarily pulled back slightly from the end plate using a pulley system that allowed the end board to rotate freely, thereby equalizing the tensions. After reseating the field planes in a superlayer, the supercells were checked for electrostatic instability at an electric field of ~2.8 kV/cm (see section 16.3). After a supercell passed the test, the end boards were epoxied directly to the end plate.

6. Gas seal

In order to eventually re-circulate a drift gas mixture containing expensive CF_4, we specified a leak rate of less than 2.36 l/min (5 SCFH) when flowing at our nominal rate of 9.45 l/min (20 SCFH). Figure 19 shows the assembled components of the gas seal, including the G10 motherboard and the aluminum gas seal extrusions. Two key factors in creating the gas seal were

1) The individual motherboards were carefully leak checked.
2) The epoxy seal between the motherboard and the extrusion and between adjacent motherboards is in a single plane with joints easily accessible to leak detectors.

6.1. ASDQ and high voltage motherboards

In order to avoid out-gassing, the motherboards are made from G10 without flame retardant. As mentioned earlier, the high voltage is connected to one end of the wire plane and the readout is connected to the other. The motherboard on the high voltage end, called the high voltage motherboard, is a bare G10 board that contains an individual socket to pin feed-through for each pin on the end boards. The feed-through is epoxied into the motherboard. A low insertion force socket manufactured by Hypertronics [27] is used in both types of motherboards to mate with the 508 μm (0.020 in.) diameter pins on the end boards.

The motherboard on the readout end is called the ASDQ motherboard, where ASDQ refers to the readout chip which amplifies, shapes, discriminates and measures charge (see section 8). This motherboard is etched from double-sided copper-clad G10 and contains 560 pF ceramic disk, leaded blocking capacitors that connect the sense and potential wires (at positive high voltage) to the ASDQ input and ground, respectively. The low voltage legs of the sense wire capacitors connect to the ASDQ daughter board through a single row socket connector. The ASDQ daughter board contains the ASDQ readout chips and resides outside the drift gas volume. Due to the large number of penetrations through the ASDQ motherboard, a Parylene coating [28] was vapor deposited onto the surface to improve the gas seal.

Both types of motherboards were leak tested using a helium leak detector. The leak rate through a single board was required to be extremely low, corresponding to a leak rate through all boards that is two orders of magnitude below the 2.36 l/min (5 SCFH) total leak rate specification for the COT. The total leak rate was therefore determined by how well we could seal around the perimeter of the motherboards. High voltage tests performed on the motherboards before installation are described in section 7.

6.2. Gas seal extrusions

The aluminum gas seal extrusions were made in 60.96 cm (24 in.) long sections by Bowers Manufacturing Company [29]. The extrusions are inserted end to end into 0.318 cm (0.125 in.) x 0.318 cm (0.125 in.) grooves that run between the slots of adjacent superlayers in the end plate. As indicated in figure 19, the extrusions actually serve several functions by providing:

- The radial borders of the gas seal at each superlayer.
- Reference to the end plate ground for the readout and high voltage electronics.

- A mount for the low voltage power and control voltages for the readout electronics.
- A mount for the cooling lines and good thermal connection to the end plates.
- A mount for the Faraday Cage, which completes the electrical enclosure around the ASDQ and high voltage daughter boards.

Copper grounding clips, with sharp protruding points, were placed around the base of the extrusion at 3.81 cm (1.5 in.) intervals before inserting the base into the slot in the end plate. The grounding clips provide good electrical contact between the end plate and the extrusion and through it to the readout and high voltage electronics. Just before insertion, the slot was filled with Stycast 2850 epoxy [30] (with catalyst 9), which has excellent thermal conductivity.

6.3. Making the gas seal

Polypropylene funnels were slipped over the socket connectors on the motherboards to help guide the pins on the end board during installation. The high voltage motherboards were plugged in first, and the DC connections to the end boards on the opposite end plate were verified. The ASDQ motherboards with the blocking capacitors were then installed, and an AC test was used to verify connections through the chamber. After all the connections were verified, we were ready to apply the epoxy around the perimeter of the motherboards.

At least a 0.318 cm (0.125 in.) border was left along the long (closer to radial) edges of the motherboards to allow for an epoxy strip to span across adjacent boards. An epoxy bead was run along the edge of each board and a 0.635 cm (0.250 in.) wide strip of Mylar was then placed on top and gently pressed until epoxy filled in completely below. Because the epoxy was applied on a vertical surface, a gel epoxy (Ace part number 18614 [31]) was used in order to prevent excessive running. The joint sealed very well, and we had little patching to do during subsequent leak checks.

The gel epoxy was also used to provide a fillet along the circumferential joint between the motherboard and the gas seal extrusion (see figure 19). This corner joint was more difficult to control, so a very thin epoxy, Epolite 5313, was brushed on after the gel had set in order to fill in tiny gaps.

At this point, we also screwed on covers over the hatches in the outer cylinder and completed the seal with Scotch-Weld 2216 structural epoxy along the corner joints and screw head wells.

The leak checking was done by flowing P5 gas (95% argon and 5% methane) through the chamber and probing for leaks using leak detectors that are extremely sensitive to methane. P5 was chosen because the mixture is not flammable. Often one could better pin point leaks by placing a syringe over the head of the leak detector and pulling a slight vacuum. Leaks were patched with fast setting DP110 [8] translucent epoxy on the motherboards and DP110 gray epoxy on the outer cylinder. Leak checking continued until the leak rate fell to ~0.47 l/min (1 SCFH), which is well below our 2.36 l/min (5 SCFH) requirement for re-circulation.

7. High voltage system

The COT high voltage is divided into 8 superlayers, each with 25 high voltage channels corresponding to the 12 sense wires and 13 potential wires. High voltage is supplied to superlayers 1, 4, 5, and 8 on the West end plate and to superlayers 2, 3, 6, and 7 on the East end plate (protons in the beam travel from West to East). Figure 20 is a schematic of the high voltage distribution for one superlayer.

7.1. BiRa power supplies, control and monitoring programs

The high voltage power supplies are the BiRa [32] VME 4877 system, which consists of a motherboard containing eight 3.5 kV, 3 mA pods. A total of 25 motherboards and 200 pods are housed in 5 VME crates. The system is controlled using a local PC running Windows NT [33], an SBS Bit3 Model 616 PCI to VMEbus adapter [34], and VMIC Model 5504 master bus and slave bus repeaters [35].

Many of the BiRa pods require a significant load to produce a well-regulated output voltage. We therefore added a separate 20 MΩ (10 MΩ) load to the sense (potential) wire pods, as shown in figure 20. This current is returned to the pod in a manner that bypasses the current monitor. A pair of Zener diodes in series (back to back) between the current return

jumper and ground prevents the jumper from charging to more than 6 volts in case it becomes disconnected from the power supply.

The protections in the BiRa system are the trip daisy chain, the pod hardware over-current limit, the pod software over-current limit, and the pot-adjustable pod over-voltage limit. All 25 pods in a superlayer are together in a trip daisy chain, since breakdowns would occur inside the chamber if pods were allowed to trip on their own. The control program on the local PC sets the levels of the hardware and software current trips. The hardware trip occurs immediately, while the software trip requires that the current exceed the trip level for a programmed number of ADC reads (each pod's current is read approximately every 40 ms). The level of the slower software trip is usually set about a factor of three below that for the hardware trip.

The control program on the local PC is written in C++, the standard CDF language for controls. In order to diagnose many types of problems with the COT, it is necessary to read and display the 200 voltages and currents approximately every 40 ms. Available graphics programs were not nearly fast enough, so the display program was written using Microsoft Foundation Classes.

The CDF IFIX [36] network communicates with the local PC to provide parallel remote control for the shift crew and a separate display to monitor the performance. The most important monitor is for trips, and IFIX produces an audible alarm and indicates which superlayer has tripped. The power supply status display on the local PC is reproduced in the control room (at a much lower refreshing rate), so that the shift crew can also record which supply within the superlayer caused the trip. In addition to the CDF trigger and data acquisition system being disabled in hardware when a trip occurs, IFIX will not allow data taking to resume until the tripped layer is back to greater than 99% of full voltage. IFIX also monitors all power supply voltages and currents (BiRa ADC readings), and will produce an audible alarm if a voltage is not within a small window around its set value (BiRa DAC setting).

The absolute pressure in the drift gas volume is monitored by four redundant pressure transducers, and subject to consistency checks, the average value is used to modify the high voltage power supply settings to compensate for the change in gas gain due to atmospheric pressure. The readings from the pressure transducers are also sent to IFIX and put directly into the data event stream for later use in off-line analyses.

7.2. High voltage crowbar box

As shown in figure 20, when a trip occurs, all 25 voltages within a superlayer discharge through a single SCR (Eupec T 201 N [37]) residing in the superlayer's crowbar box. The purpose of the crowbar box is to bring down the COT high voltage as quickly as safely possible if some harmful (or potentially harmful) condition is detected and to prevent multiple discharges on a single wire due to the energy stored in other wires in the COT.

Inside the crowbar box, the 25 channels are connected together through high voltage diodes, which isolate them during normal operation, and current limiting resistors. The highest voltage channel (the sense wire at the largest radius) draws ~10 μA due to SCR leakage. The current limiting resistors were chosen to limit the peak discharge current to 100 A, and the RC of the discharge ranges from 200 to 400 μs, depending on the superlayer. The SCR is triggered by a TTL active low signal on the BiRa trip daisy chain.

The superlayer is divided into quadrants with equal number of supercells at the crowbar box. The rear panel has 125 SHV connectors in 25 columns of five connectors each. Each column of five connectors is bussed together and corresponds to a specific sense or potential wire in the superlayer. One of the five connectors is for the cable from the power supply channel and the others fan out to the four quadrants.

7.3. High voltage filter box

For each superlayer, 100 RG58 cables run from the crowbar box down to the End Wall of the CDF detector, and the 25 cables for each quadrant are routed to the relevant corners. There they connect to the input of the high voltage filter box, as shown in figure 20. Input to the filter box is via an SHV panel feed-through connector, and a G10 panel is used in order to insulate the shield from detector ground.

Filtering is done with 1000 Ω in both the supply and return (ground), followed by a 1 nF capacitor between the two. After the filter, the grounds of all the sense and potential wires in the superlayer are tied together. The value of the filter resistors was chosen to limit the maximum voltage drop across them under normal operation to less than one volt. In parallel with these resistors are high current diodes that limit the voltage in the reverse direction during fast discharge (maximum of about 1 A) to about one volt.

The filter box delivers all voltages for the sense wires in a given superlayer to a header for a flat silicone ribbon cable that carries the power through the "30° crack" between the Plug Calorimeter and the End Wall to the COT (see figure 1). All voltages for the potential wires are delivered to a similar header. In order to protect the ribbon cables from accidental over-voltage between adjacent conductors, varistors with 2500 A maximum peak current were attached between adjacent sense wires and another set between adjacent potential wires. The varistors limit the maximum voltage difference to about 1000 volts, a safe operating condition for the ribbon cables alone.

7.4. Silicone ribbon cables and daisy chains

The silicone ribbon cable has 14 conductors with 1.27 mm (0.050 in.) pitch and is suitable for mass termination. Cables from the four superlayers at the filter box are wrapped together in an insulated and shielded bundle in order to make the run through the 30° crack. The ribbons are individually wrapped with 25.4 μm (0.001 in.) Kapton. The quadrant bundle is wrapped with 50.8 μm (0.002 in.) Kapton, copper cloth (with copper ground braid), and finally a tough polyolefin jacket. The ground braid is soldered to copper cloth at 30 cm (12 in.) intervals along the entire 7.62 m (25 feet) run and is screwed to the outermost gas seal extrusion on the COT.

At the chamber face, the ribbons are connected to daisy chains made of the same cable. The daisy chain distributes high voltage to the individual cells in a quadrant of a superlayer. The sense wire daisy chain connects to the high voltage daughter board on the outer diameter of the superlayer and the potential wire daisy chain connects on the inner diameter.

7.5. High voltage daughter board, testing of boards

As shown in figure 20, the daisy chain ribbon connects to the high voltage daughter board (HVDB). A photograph of the HVDB is shown in figure 21. The high voltage is connected to the sense (potential) wires through 100 kΩ (200 kΩ) Dale [38] metal film CCF-07 ¼ watt resistors. A silicone coating is poured over the resistors to prevent breakdown between neighboring channels on the board.

The HVDB provides the termination of the sense wires for chamber pulses via the 300 Ω Dale CCF-60 ½ watt series resistor and the 560 pF Xicon [39] 6 kV, Y5P, leaded, ceramic disc blocking capacitor to ground. The potential wires are terminated directly through the blocking capacitor to ground. As indicated in figure 20, the ASDQ daughter board provides the ~300 Ω sense wire termination on the readout end.

The HVDB components were tested to survive simulated chamber breakdowns, which included the charge stored in the blocking capacitors. The HVDBs, high voltage motherboards and ASDQ motherboards were tested overnight for discharge at voltages far in excess of their normal operating values (all sense wires at 5000 V and all potential wires at 3500 V). Boards were also tested for current leakage with both the sense and potential wires at 3500 V, and those with leakage in excess of 1 nA were rejected.

7.6. Choice of High voltage Components

The 3.5 kV maximum voltage of the BiRa pod was chosen to allow operation at a drift electric field of 2.5 kV/cm. The maximum projected current draw from a pod is that for superlayer 1 sense wires at a luminosity of 4×10^{32} $cm^{-2}sec^{-1}$: 8.9 μA/wire x 168 wires = 1500 μA. This current, plus the 175 μA drawn by the 20 MΩ stabilizing load, is comfortably within the 3 mA capability of the pod.

At the maximum current for SL1, the voltage drop across the 100 KΩ series resistor per wire and the 1 KΩ series resistor per quadrant is 1.3 V. Therefore the voltages at the wires will not sag appreciably as the luminosity increases. We could afford to increase the series resistance per potential wire to 200 KΩ and still avoid a harmful voltage imbalance during a

crowbar discharge. As mentioned earlier, the value of the current limiting resistors in the crowbar box was chosen to limit the peak current during discharge to 100 A. The crowbar discharge RC of 200 to 400 μs is fast enough to prevent multiple sparking in case of a sense wire breakdown.

Several considerations contributed to the choice of the blocking capacitor on the HVDB and ASDQ motherboard. The CTC used a leaded ceramic capacitor with voltage rating a little less than a factor of two above the maximum operating voltage, and we did not have a capacitor fail during 10 years of operation. We therefore expect the 6 kV leaded ceramic capacitor used in the COT to be very reliable (there have been no failures to date). The voltage coefficient of this particular capacitor is quite good, with the 560 pF value at zero voltage dropping to 360 pF at a typical sense wire high voltage. The capacitance at high voltage is sufficient not to alter the pulse shaping and provide an effective bypass for high frequency noise.

8. ASDQ chip and ASDQ daughter board

The front-end readout electronics includes the ASDQ daughter board (with the ASDQ chips), micro-coax ribbon cable, repeater board, flat cable, and TDC96C TDC. A schematic of the readout chain is shown in figure 22. The ASDQ daughter board connects to the wire plane through the ASDQ motherboard, which provides the gas seal.

The ASDQ chip [40] is an extensive re-design of the ASD8 chip, which was originally designed for an SSC detector and has been used in several experiments since then. The ASDQ chip provides input protection, amplification, shaping, baseline restoration, discrimination, and charge measurement for eight sense wire channels. Figure 23 is a photograph of the ASDQ daughter board. It provides more input protection and distributes power, control voltages, and the calibration signal to three ASDQ chips (24 channels) on board.

The chamber gain and discriminator threshold can be externally adjusted at any time, but for purposes of describing the properties of the ASDQ chip, we will use operating values close to those at the beginning of Run 2. The COT gain is ~2×10^4 and GARFIELD [41] predicts that the average chamber pulse for a radial minimum ionizing particle (MIP) will provide ~10 fC into the ASDQ during its 8 ns peaking time. We will call the charge into the ASDQ during the peaking time Q. Q varies considerably due to fluctuations in ionization and differing particle trajectories, so the discriminator threshold should be set as close to the inherent noise level as practical to ensure high hit efficiency and good timing accuracy.

When attached to the COT (10 pF stray capacitance + COT + far end termination resistance), the inherent rms noise of the ASDQ is ~3800 electrons. We are presently operating with a discriminator threshold, referred to the ASDQ input, of 2.3 fC (14,350 electrons). Most of the chamber could run with thresholds near 1.7 fC without introducing noise hits into the readout. Table 4 lists some other specifications of the ASDQ chip.

8.1. Input protection and preamplifier

The off-chip input protection on the ASDQ daughter board consists of a 25 Ω series resistor and a diode to ground to protect against large negative spikes. The on-chip protection includes more series resistance into large area diodes for both negative and positive spikes.

There are two preamplifiers in each channel to provide a pseudo-differential input. The preamplifier is a three transistor, cascoded, common-emitter circuit. It has a gain of 1.5 mV/fC, is linear to Q = 1.5 pC, and has a 1.5 ns rise time.

8.2. Shaper and baseline restoration

The shaper is fully differential and has two-stage multipole shaping to cancel the positive ion and preamplifier tails. The shaper has a gain of 25 mV/fC, a range of Q = 600 fC for the ion tail stage, a range of Q = 120 fC for the preamplifier tail stage, and a shaping of 5 ns (0–peak) at the baseline restorer (BLR) input. The undershoot of the pulse at the BLR input is less than 2%. In case one wishes to run with higher chamber gain, there is a selectable ×2 attenuator that reduces the amplitude of the pulse into the second stage of the shaper.

The BLR is fully differential and its AC coupling removes DC process variations before the

discriminator, thereby producing very uniform channel-to-channel discriminator thresholds. The BLR allows for high rate performance and provides insensitivity to tail cancellation imperfections. For large charge deposition (greater than 30 MIPs), it allows earlier re-triggering and eliminates multiple triggers when tail cancellation is saturated. The BLR was designed to minimize the effect on the charge measurement. There is an analog monitor point for channel 8 that provides a copy of the BLR output.

The gain of the BLR is ~66% for Q = 3 fC and 90% for Q > 30 fC. The range is Q = 120 fC, and there is no significant additional shaping for large pulses. The under shoot is < 3 fC for Q < 100 fC.

8.3. Discriminator and Q measurement

The discriminator threshold is computer controlled and allows triggering down to Q ≈ 2 fC. The time slewing is less than 1 ns per decade of overdrive. The minimum output width is 5 ns. The internal offset is less than 1 mV (0.05 fC). The threshold range is 10 fC, and the threshold is uniform to 10% from chip to chip. The output is bi-level LVDS.

There is a computer controlled enable for the measurement of Q, in which the output width becomes proportional to log Q. When enabled, the circuit switches from fast (8 ns) shaping below threshold to ~28 ns shaping for charge integration above threshold. Once the signal falls below the trailing edge threshold, the circuit again switches back to the short integration time. In practice, the Q measurement is very insensitive to the trailing edge threshold and this value is fixed by components on the ASDQ daughter board. The Q measurement resolution and the pulse width are quite sensitive to the capacitor drain current, so it is also computer controlled.

8.4. Calibration circuit of the ASDQ chip

The calibration circuit allows the determination of relative t_0 and the Q versus width relation for individual channels within the ASDQ chip. It provides for a separate programmable pulse up to Q ~ 30 fC to the preamplifier inputs for even and odd channels.

The calibration trigger pulse to the ASDQ chip is differential ECL with a minimum width of 5 ns. The generation and distribution of the trigger pulse and the COT calibration program are described in section 11.

8.5. Fabrication and layout

The ASDQ chip uses the MAXIM [42] SHPi Analog Bipolar Process, which is well characterized and radiation tolerant. The chip layout was done with the MAXIM Quickic8 Layout Tool, which provides good isolation to minimize cross talk and conservative "in-house" design rules for high yield. HSPICE was used to simulate the circuit.

8.6. ASDQ tests with a single-cell prototype in 14.1 kG field.

Features of the chip design were tested with HSPICE using simulated chamber pulses on the input. The design was also checked using pulses from a chamber operating under realistic conditions. A small prototype with a single supercell was built in order to test components, including the ASDQ chip design, with cosmic rays in a 14.1 kG magnetic field, the nominal field for running the COT in CDF.

Data were taken using a preamplifier from the CTC and pulses were recorded on a LeCroy 7200 digital scope with 1 ns sampling. HSPICE was used to de-convolute the effects of the CTC preamplifier and the resulting "raw" chamber pulses were fed into the input of the ASDQ HSPICE simulation.

Figure 24 shows the signal evolution in the ASDQ HSPICE simulation for a radial cosmic ray track with Q ≈ 80 fC. Moving from top to bottom, the traces show the signal at the preamplifier input, preamplifier output, shaper output, BLR output and discriminator output (without and with the Q measurement enabled). One notes the absence of shaping by the preamplifier, the effective cancellation of the positive ion and preamp tails by the shaper, and the slight undershoot and minimal affect on the shaping caused by the BLR. Finally, one notes the significant increase in the discriminated pulse width when the Q measurement is enabled with a small capacitor drain current. During early data taking with the COT, we optimized the performance by adjusting the chamber

gain, discriminator threshold and capacitor drain current.

8.7. ASDQ tests with a high rate prototype

Chamber measurements were made with the pre-production versions of the ASDQ chip and daughter board primarily to test how well the BLR handles high rates on the sense wires. A full-length prototype with two supercells and thin windows for irradiation with Sr^{90} sources was constructed for this purpose. The measurements employed a cosmic ray trigger using scintillation counters and an un-radiated straw chamber stack to point to the road where hits from the cosmic ray were expected in the prototype.

Both the ASD8, the earlier version of the chip without baseline restoration, and the ASDQ were used to read out the two cells. Figure 25 shows the counting rate on a central wire as the number of Sr^{90} sources is increased from one to seven. The activities of the sources were very uniform, and each induced a current of ~1 μA/wire (recall that a sense wire in superlayer 1 will see a current of ~8.9 μA at the projected maximum Run 2 luminosity of 4×10^{32} cm^{-2} s^{-1}). As indicated in Figure 25, the ASD8 becomes quite inefficient at counting small charge depositions when using more than three sources, and there is a large improvement with the ASDQ.

One expects the position resolution to degrade when the rate on the wire becomes high due to hit masking and baseline shifts. When looking at tagged cosmic rays with no sources, the per-hit rms resolution was 150 μm when using either the ASD8 or ASDQ. As the number of sources was increased to seven, the rms resolution increased by 100 μm for the ASD8 and by 60 μm for the ASDQ.

8.8. Production and testing of the ASDQ chip and daughter boards

The ASDQ chip production order to MAXIM was for 37 wafers, and 6600 chips passed the basic quality requirements (89% yield). The distribution of measured thresholds for a 3 fC injected charge is shown for the 6600 chips in figure 26. In order to optimize threshold uniformity, ~4300 chips were selected from the central portion of the distribution to mount on the ASDQ daughter boards.

Figure 27 shows the width distribution for the 6600 chips when the Q (dE/dx) measurement is off and on. In this case, the injected charge on the input is 20 fC. One notes the increase in pulse width with the Q measurement on. The channel-to-channel uniformity in width is extremely good (0.5 ns rms) with the Q measurement off or on.

A total of 1434 ASDQ daughter boards were assembled by SUBTRONICS [43]. The boards went through several levels of checks and burn-in:

- Level 1 (93.9% passed): Visual inspection and test basic properties of the board.
- Level 2 (97.3% passed): Check functionality of board and measure thresholds and output widths of the signals from each channel.
- Burn-in for one week.
- Level 3 (98.3% passed): Same as Level 2 tests.

The thorough testing has proven to be very successful, since only a handful of boards have had any sort of failure during the initial running.

9. Power and control voltages for the ASDQ

A schematic of the distribution of the low voltage power and control voltages to the ASDQ daughter boards is shown is figure 28. In this section, some of the components will be described, starting with the Low Voltage Filter Box.

9.1. Low Voltage Filter Box

In order to run at low thresholds, the ASDQ requires a quiet source of power. Similar to the high voltage, the low voltage power is distributed to quadrants of cells in four superlayers from Low Voltage Filter Boxes that are mounted at the corners of the CDF detector End Walls. A Low Voltage Filter Box contains the primary power supply (AC to DC converter), filters, fan-outs and over-current protection circuitry.

The primary power supply is a VICOR FlatPAC switching supply [44], which is capable of supplying 40 A at +3.3 V and 60 A at –3.3 V. There is a disable function that is used to shut down the supply remotely when there is an over-temperature condition

at the supply or a failure of the ASDQ cooling system (see section 12.2).

The switching noise is of a frequency and magnitude that affect the ASDQ performance, so filtering is provided. The current passes through a Dale 24 μH, 60 A inductor (1HV-60-24 [38]) followed by a 330 μF capacitor. The voltage regulation is done after the 24 μH inductor in order to eliminate the uncertainty due to its voltage drop.

The current is fanned out to quadrants (or sometimes octants) of cells in four superlayers, such that no channel draws more than 6 A. The current from each channel passes through a power inductor with resistance ≈ 7 mΩ, and an Analog Devices [45] CMP04 comparator monitors the voltage across the inductor.

The comparator is biased so that it will generate a trip signal at the desired (pot-adjustable) level indicating an over-current condition. The over-current condition causes a flip-flop to latch in the off state, which in turn opens an Omron G4W relay [46] through which the current normally passes. A varistor protects the relay contacts from arcs caused by opening with an inductive load. The "active" current trip described here has an obvious safety advantage over fuses or thermal circuit breakers with fixed values, since it can be set very precisely and is fast (order of a second) even for only a few percent over-current.

The +5 V supply that powers the normally open relays is also used to generate the current to disable the VICOR power supply. If the +5 V power is interrupted, the relays will open preventing power from reaching the chamber even if a harmful condition (local over-temperature or ASDQ cooling system failure) occurs.

A pair of parallel toggle switches can put the flip-flop for each channel into a tripped or reset state. One is local on the front panel of the Low Voltage Filter Box and one is remote in the first floor control room. The toggle switch not in use is kept in the neutral position.

9.2. Distributing power to the ASDQ daughter boards

There are a series of seven cable (or bus) segments, usually connected by butt splices, that carry the low voltage power from the Low Voltage Filter Box to the Circumferential Voltage board (CV board) on the end plate. The purpose of the many segments is to keep the cable cross section as large (and the voltage drop as low) as practical, in order to help minimize the possibility of oscillations. The bulk of the run is in two segments. The first uses 3.4 m (132 in.) long AWG 8 cable between the area of the Low Voltage Filter Box and the 30° crack , and the second uses 2.6 m (102 in.) long AWG 10 square copper bus through the 30° crack to the end plate. In both segments, 3 (2) (1) parallel conductors are used for –3 V, +3 V, and ground, respectively.

The CV board can be seen in the assembly view of the end plate gas seal and readout in Figure 19. The CV board carries the low voltage power and the control voltages to the ϕ location of the ASDQ daughter board, and at that point a short ribbon jumper [28 gauge conductors with 1.27 mm (0.050 in.) pitch] connects between the CV board and ASDQ daughter board. As seen in figure 19, in order to limit the voltage drop, the low voltage power is carried on copper busses that are screwed to the CV board.

9.3. Control voltages: DAC and buffer board

The six computer adjustable control voltages of the ASDQ chips are for threshold (DTHR), odd channel calibration level (TREFO), even channel calibration level (TREFE), Q measurement enable (QEN), Q measurement capacitor drain current (QDR), and the ×2 attenuation option before the second amplification stage of the shaper (ATN). They are all generated by VMIC [35] 4132 DAC modules that reside in one of the TDC VME crates in each of the End Wall corners. Separate control voltages are generated for each quadrant of each superlayer, and they are buffered on the chamber face by the buffer boards.

There is one buffer board for each low voltage power channel (one per quadrant for superlayers 1 – 3, and one per octant for superlayers 4 – 8). The DAC voltages are routed through the Low Voltage Filter Box, where they pick up ± 5 V lines to power the buffer boards and are sorted into separate ribbon cables for each superlayer / quadrant. The ± 5 V lines are protected with fuses.

The superlayer / quadrant (or octant) ribbons plug into the buffer boards, which are mounted between a pair of ASDQ daughter boards in that quadrant (or octant). The buffer board contains an MC33076 op-amp [54] for each control voltage, and the op-amp is capable of delivering 100 – 150 mA of current, depending on the voltage. In additional to isolating the control voltages from the outside environment, the op-amp is necessary to supply sufficient current for DTHR, since the DAC is not capable of doing so.

As shown in figure 28, the control voltages are connected to the CV board through a short jumper cable. This jumper also brings the –3 V from the CV board bus to the buffer board, where it serves as the reference voltage for the TREFE and TREF0 calibration pulse height levels. The control voltages are distributed to the ASDQ daughter boards on 889 μm (0.035 in.) wide × 99 μm (0.0039 in.) thick copper traces on the CV board (equivalent to 28 gauge), except for DTHR, which has a 0.533 cm (0.210 in.) wide trace to reduce the voltage drop.

9.4. Monitors for power and control voltages

ASDQ power and selected control voltages (DTHR and QDR) are directly monitored from quadrant (or octant) CV boards through 1 KΩ series resistors. The voltages are routed to CAMAC 3527 Kinetic Systems Scanning ADCs [56], which are read out by the same PC that controls the high voltage power supplies. The CDF IFIX monitoring program reads and displays the values and produces an audible alarm if they are out of tolerance.

10. Micro-coax, repeater board, flat cable, TDC

As shown in figure 22, the output logic signals from the ASDQ are carried on micro-coax cables to the repeater boards that sit just outside the 30° crack on the End Wall Hadron Calorimeter (see figure 1). Flat ribbon cables with larger conductors and less signal dispersion than the micro-coax carry the signals a significantly greater distance from the repeater boards to the TDCs.

10.1. Micro-coax cable

In order to run at low threshold, the ASDQ requires a shielded cable for the LVDS output signals. In addition, there are severe space constraints in the cable slots passing through the 30° crack, so a cable with very small cross section is required. We tested two cables that would fit: a custom micro-coax cable that was used by the VTX in Run 1 and a shielded twisted pair manufactured by Habia Corporation [47]. The transmission properties of the micro-coax pairs were slightly better, and the cable was more readily manufactured at the time, so we chose to use the micro-coax.

The micro-coax properties are:

- 7/44 gauge silver plated pd135 copper
- 106.7 μm (0.0042 in.) clear FEP to 355.6 μm (0.014 in.) nominal OD
- 4-5-44 silver plated spiral shield
- 50.8 μm (0.002 in.) black FEP jacket to 558.8 μm (0.022 in.) nominal OD
- 40 Ω characteristic impedance
- Attenuation @ 100 MHz less than 34 db for 30.48 m (100 feet).

The conductors are woven into flat ribbons of 25 conductors, and two ribbons are used to read out each ASDQ daughter board (48 conductors for signals and two for the calibration trigger). Bay Associates Incorporated [48] manufactured the cables.

The average length of a micro-coax ribbon is 3.96 m (13 feet), and they were hand terminated on each end. On the ASDQ end, they were terminated onto a board with a socket connector, which can be unplugged from the ASDQ daughter board. On the other end, they were soldered to a termination board, which in turn was soldered to the repeater board.

10.2. Repeater board and flat cable

The repeater board serves to amplify the signal and to provide a ground break between the ASDQ and the TDC. Each differential signal is put through a long-tailed transistor pair amplifier with current source (Intersil [49] HFA3102 dual array). A current mirror transistor in a HFA3127 transistor array package sets the standing current in each transistor pair to ~5 mA. Each card “repeats” the signal for 24 channels (the output of two cells or one ASDQ

daughter board). The ~50 Ω pull-up resistors for the collectors of the transistors are located in the TDC module, which also supplies the –3 V power for the current sources on the repeater board.

The 7.62 m (25 feet) long cable connecting the repeater board to the TDC is a 60 conductor, 0.635 mm (0.025 in.) pitch, 30 gauge ribbon cable with a copper mesh ground plane manufactured by Amphenol-Spectra-Strip [50]. The cable is suitable for IDC termination. The ribbon cable is set up as follows: 48 conductors are used for the 24 signal pairs, 2 conductors are used for the calibration trigger pulse, 6 conductors are used for ground and 4 conductors are used for the –3 V power for the current sources on the repeater board. The –3 V power is protected by a 1.5 A circuit breaker in the TDC.

10.3. TDC

The Michigan TDC96C TDC is described elsewhere [2]. The version with LVDS input is used to read out the COT and hadron calorimeters, and the version with ECL input is used to read out the CDF muon chambers. The board uses 96 of the JMC96 TDC ASICs, which record the arrival time of a pulse's leading edge and trailing edge in 1 ns bins.

Wire data from the repeater cards is received by differential LVDS receivers and fed to the JMC96 TDC chips. On the JMC96 chip, the wire data enters a 5.6 μs delay chain in 1 ns steps. A Level 1 Accept from the trigger directs the oldest data into one of four buffers for storage during Level 2 trigger processing. Each of these buffers holds 2.0 μs of wire data. A Level 2 Accept causes the JMC96 to digitize this 2.0 μs of data and store the times of edges in a single on-chip FIFO. An on-board DSP empties the entire FIFO and re-formats the pulse information in a selected time window into a leading edge time and width. For COT operation, the TDC is programmed to transfer up to eight hits per wire through the remaining DAQ. The DSP also performs a channel dependent t_0 subtraction and channel identifier assignment using constants from on board FRAM.

The TDC also routes hits directly from the input differential receivers to a daughter board for input to the Level 1 trigger. On axial layers, this daughter board detects the presence of an early and/or late pulse in the drift time window, multiplexes this information for two sense wires to match the available cable plant from the detector to the control room, and ships the information to the XFT, the eXtremely Fast Tracker [51]. The XFT finds charged tracks in 48 p_T bins in time for use in Level 1 trigger decision.

As noted in section 11, the calibration trigger signal passes from the back plane of the VME crate through the TDC to the flat ribbon cables. The only processing of the calibration signal by the TDC is a translation from PECL to ECL logic levels.

11. Calibration of the readout electronics

When a TDC is installed, a calibration internal to the crate is performed by the TRACER, which generates and sends pulses along the VME crate back plane to the TDC's JMC96 chip inputs. This is a good test of the functionality of the TDC, but additional hardware is needed to test and calibrate the entire readout.

11.1. COT calibration network

The COT calibration network is used for three purposes:

- Diagnostics: Test all connections and the ASDQ functionality. Present the results in a manner to help debug problems with the readout.
- t_0 calibration: Map the channel-to-channel relative timing to an accuracy of 0.5 ns.
- dE/dx calibration: Map the Q measurement (i.e., pulse width) as a function of injected charge for each ASDQ channel.

The 0.5 ns accuracy requirement of the t_0 calibration program corresponds to a position uncertainty of ~25 μm when using a gas without CF_4 and ~45 μm when using a gas with 15% CF_4, as envisioned if the time between bunch crossings is reduced from 396 ns to 132 ns.

Figure 29 shows the calibration network. The Calibration Interface Card (CIC) is used to produce the calibration trigger pulse in synchronization with the CDF clock. The pulse fires the BNC950 VME programmable delay generator (PDG) [52], and its

NIM output is fanned out 8-fold with identical timing as differential PECL signals, which are carried by pairs of 67.1 m (220 feet) long coax cables to the eight corners of the CDF detector.

In each corner a fan-out further copies three-fold with identical timing, and each copy is carried as differential PECL over short [~1.2 m (4 feet)] Twinax cables to a TRACER module in each of the VME TDC crates. The TRACER puts the calibration trigger signal onto the back plane, from where each TDC receives it and sends an ECL pulse to the flat cable, repeater board, micro-coax and finally the ASDQ calibration trigger input. A calibration pulse of programmed level (TREFE and TREFO) is subsequently injected into the pre-amp and the ASDQ output returns to the TDC along the same path as the COT signal.

In order to meet the calibration goal, the relative arrival times of the calibration trigger pulse at each ASDQ must be known to an accuracy of 0.5 ns. This is accomplished by: 1) tuning the network so that the pulses arrive at the TRACER inputs simultaneously and 2) measuring the relative delays from the TRACER inputs to the 1260 ASDQ daughter boards for entries into a correction "cable length" database. The components must be stable over the course of the delay measurements and subsequent calibration data taking, which in practice means stable over the course of the run. Variations due to temperature, humidity, or aging effects are minimized.

11.2. Specifications of some key components

The eight long coax cables are LMR-200-FR cable (FR refers to flame retardant), which is made by Times Microwave Systems [53]. It is an RG-58 sized, 50 Ω cable that accepts BNC connectors and has a propagation velocity of 0.85c. The propagation delay was measured to change by 40 ps / ° C for 304.8 m (1000 feet). The eight cables split up for only the last 24.4 m (80 feet) of their run, and the maximum temperature difference after the split is ~8° C. Since only their relative timing is important, the temperature dependence corresponds to a maximum relative time difference of 26 ps at the input to the 1:3 fan-outs. The affect of a 40% change in relative humidity is even smaller.

The fan-out modules use Motorola MC100 series parts [54], which are supply voltage and temperature compensated. Each output of the 1:8 fan-out has a capacitor in parallel with the 50 Ω back-termination in order to compensate for the high frequency attenuation in the long coax cable. Both the 1:8 and 1:3 fan-outs are built as 9U VME boards.

Combining contributions from both cables and fan-outs, the total spread of arrival times at the TRACER inputs is ~350 ps, and the relative arrival times should change by less than 100 ps over the course of the run.

11.3. Cable length database

Initial entries into the cable length database were determined by measuring the time delays between a pulse injected into the TRACER input and its arrival at the ASDQ daughter boards. After the 1260 measurements were completed, an optimization of the VME back plane termination was performed, which produced up to a 3 ns change in the propagation delay to a TDC slot. There was an opportunity to measure the change in propagation delay for a few crates, and a functional form was fit to these measurements to correct data from all TDC crates.

It was necessary to make further corrections using high quality fit tracks to reduce the error in the channel-to-channel t_0 variation below the desired 500 ps. Using channel-to-channel t_0 variations with the physically measured cable length correction database as input, STAGE0 (see section 15.2) determined an optimal set of drift constants (e.g., drift velocity and Lorentz angle). The unsigned residuals from the fit tracks were averaged over a cable and used to correct the cable length database for future use.

11.4. Calibration programs

The t_0 calibration, dE/dx calibration, and the Diagnostics program all run as "X-mode" calibrations, which means that the data out of the TDCs are processed in the crate CPUs. The procedure is to set the desired delay and DAC values and send calibration trigger pulses for the desired number of readout cycles. For each cycle, the hits are converted to words of leading edge time and width by

the TDC DSP code. After the readout cycles are completed for that set of delay and DAC values, the times and widths are processed in the crate CPUs.

In the case of the t_0 calibration, for each channel the crate CPU calculates the average and rms for both time and width and the average occupancy. It loads these into a data bank that is made available to a Consumer program. The Consumer program makes quality checks on the data, substitutes t_0 values from nearby channels if the calibration for a channel fails the checks, applies the correction from the cable length database, compares these t_0 values to those currently in the database used by the analysis code, and substitutes the new calibration results if there is a significant change.

The Diagnostics program tests the chamber wire connections, ASDQ functionality, and the remainder of the readout. It categorizes problems to facilitate repairs. An example of a less than obvious use is the detection of a gap in the connection from the ASDQ input, through the sense wire, to the 300 Ω resistor and blocking capacitor on the high voltage daughter board. The program issues pulses of uniform height to all channels and increases the ASDQ threshold until only 50% of the hits are counted. If there is no connection to the chamber wire, the pulse height into the ASDQ for that channel is twice as large and the threshold at 50% counting rate will double.

12. Temperature controls and monitors

Systems dealing with temperature controls (this section), drift gas distribution (section 13), and the nitrogen safety purge (section 14) are part of the general infrastructure of support for the various subsystems in the CDF detector [2]. This paper will emphasize aspects specific to the COT.

The COT aluminum end plates were machined and aligned under strict temperature controls: a total window of 3° F around 69° F. In addition to the tracking distortions that would be caused by the expansion or contraction of the end plates due to large temperature excursions, one also has to worry about the myriad of epoxy joints between various types of materials breaking under thermal stresses. In addition, the major heat source, the ASDQ chips, will have a reduced lifetime if operated at too high a temperature.

Inside the closed End Plugs, there are several sources of heat and refrigeration. The heat sources are the ASDQs, which produce ~1200 W, drift gas heating due to positive ions, ~270 W @ 4×10^{32} $cm^{-2}s^{-1}$, and TOF preamps and phototube bases, ~900 W. The solenoid's cryostat is a several-hundred-watt refrigerator. The silicon detector is also a net refrigerator, due both to un-insulated cooling lines running across the COT Faraday cage to the detector and to the active volume itself. The amount of net refrigeration depends on the cooling fluid temperature, which can vary from 15° C to –6° C, and the fraction of the detector that is powered.

12.1. Silicon heaters and TOF heaters

In order to have control of the COT temperature at the inner diameter under widely varying conditions, the outside of the Intermediate-Silicon-Layers support tube, which encloses all of the silicon detectors shown in figure 1, was wrapped with Mylar bubble insulation with a very thin [~25.4 μm (0.001 in.) aluminum skin. The bubble wrap reduces the potential refrigeration to less than 100 W. Outside of the bubble insulation are mounted heating sheets of copper traces on Kapton (mostly near the bottom), and current through the traces is controlled to mitigate the remaining cooling and keep the COT inner cylinder near 70° F.

Since the TOF system is normally a large net heat source, their heaters never come on unless essentially all power to the region is turned off, leaving only the solenoid cryostat to cool things down.

12.2. SUVA cooling

Heat from the ASDQs, the TOF bases and preamps, and positive ions is partly (possibly ~20%) mitigated by cooling from the cryostat and silicon cooling lines, but the bulk is removed by DuPont SUVA 9100 refrigerant [55] that circulates through 0.635 cm (0.250 in.) diameter, 508 μm (0.020 in.) wall stainless steel tubes mounted in the gas seal extrusions (see figure 19). SUVA 9100 is a non-flammable mixture of two chemicals, CH_2F_2 and

CHF_2CF_3, and is accepted as environmentally friendly by the EPA.

The piping system, including stainless steel lines and VCO fittings, is designed for 2414 kPa (350 psig) to contain the refrigerant during warm weather shutdown periods. The refrigerant is normally run with boiling point near 65° F [~1241 kPa (180 psig)] in order to keep the average end plate temperature near 70° F. The temperature is regulated by six RTD temperature probes inserted 0.635 cm (0.250 in.) deep into the end plates between superlayers 4 and 5 (three RTD probes equally spaced in ϕ on each end plate). Key flows and pressures in the SUVA cooling system are monitored by IFIX and will produce alarms if they fall outside acceptable limits.

There are cooling loops in eight of nine gas seal extrusions on each end plate. A cooling line enters and exits the extrusion at the same ϕ location (making a full circle), and these ϕ locations are all near the horizontal (on each end plate, four are near $\phi = 0°$ and four are near $\phi = 180°$). Entering and exiting near the horizontal optimizes the flow characteristics. Moving out in radius, the fluid alternates between first flowing through the top and bottom halves of the end plate; thereby producing a uniform cooling over the surface of the end plate. Typical temperatures at the surface of the ASDQ chips range from 90 to 93° F, which are well below values that may cause a reduced lifetime.

12.3. Temperature monitors

Approximately 80 temperatures are monitored on the COT and in the Low Voltage Filter Boxes using Analog Devices [45] AD592 temperature probes. Temperatures are monitored on the inner cylinder, the outer cylinder, the ID and OD of each end plate, the ASDQ chip surface, and more. Thirty-two representative temperature readings are tested in hardware for exceeding limits that indicate a failure of the cooling system. If any fail, all ASDQ VICOR power supplies are automatically disabled. All supplies are also disabled if the end plate RTD temperature probes from the SUVA cooling system average over 75° F. If the temperature at the surface of a VICOR supply exceeds ~140° F (e.g., due to a fan failure), a Klixon opens and only that supply is disabled.

In addition to these automatic over-temperature protections, all 80 AD592 probes are read into CAMAC 3527 Kinetic Systems Scanning ADCs [56], which are read out by the PC that controls the high voltage. A program on the PC checks if the temperatures are below or above acceptable limits, displays the temperatures and the limit check failures, and transfers the temperatures and the limit checks to the CDF IFIX monitoring program. IFIX displays the temperatures and generates an audible alarm if one is out of tolerance. For example, an alarm is generated if a temperature probe at the inner cylinder reads below 60° F or above 80° F. The high limits are tighter than those that automatically disable the VICOR power supplies, so there is a chance to correct problems before the system shuts down.

13. Drift gas system

Much of the drift gas system that is unique to the COT is shown in figure 30, the schematic from the IFIX computer control page. The equipment in the figure is located on the CDF gas platforms, and not shown are the lines making the ~45.7 m (150 feet) run to the COT and those making a similar length run back to the platforms. The cold traps, activated charcoal filters, split flow, alcohol bubbler, copper wool assimilation trap, and stainless steel wool assimilation traps are all features that are primarily motivated to reduce wire aging [57]. Section 17 describes the Gas Monitor Chambers, which monitor for aging at several points in the gas distribution.

13.1. Cold trap and charcoal filters

The cold trap uses liquid nitrogen and heaters to maintain a temperature of –110° F inside a coil of tubing through which the gas passes. This is safely above –124° F, where ethane would condense under conditions in the trap. As discussed in reference [57], a similar cold trap greatly reduced wire aging in test chambers using CDF argon / ethane from Run 1.

After exiting the cold trap, the gas passes through a coil of tubing to bring it back to room temperature and then through a pair of activated charcoal filters, which remove oils from the gas. As with the cold

trap, when using argon / ethane from Run 1, test chambers saw significantly less aging when the gas passed through these filters.

13.2. Adding alcohol to the gas mixture

As described in [57], in Run 1 the entire 14.2 l/min (30 SCFH) CTC flow passed through an ethyl alcohol bubbler, and an extremely high wire aging rate, 100k% /C/cm, was observed in a test chamber placed in the gas flow ~1 m downstream from the bubbler. The aging reduced significantly when the test chamber was moved farther downstream.

Assuming that aerosols were causing the problem, a heated copper wool assimilation trap was added at the bubbler exhaust, and the flow was split before entering the bubbler so that only ~2.36 l/min (5 SCFH) passed through the bubbler (with temperature set appropriately higher), thereby greatly reducing the agitation in the bath. After these changes were made, the aging rate of the test chamber just downstream of the bubbler was reduced to ~50% /C/cm.

As seen in figure 30, both the split flow and heated copper wool filters have been retained for Run 2. In order to maintain a stable alcohol concentration, the flows are regulated using a feedback system with mass flow meters and solenoid valves. The COT uses isopropyl alcohol in the bubbler, and the flows and bath temperature shown in figure 30 give an alcohol concentration, after the flows combine, of 1.7% (equivalent to sending the entire flow through a bath at 6° C). Adding isopropyl alcohol to the gas mixture reduced the aging rate in test chambers using argon / ethane from Run 1 by a factor greater than 5 [57]. The alcohol also allows the COT to be run at a higher voltage before the onset of glow.

The measured flow rate of the drift gas through and around the alcohol bubbler and the bubbler itself are monitored by IFIX. An audible alarm will sound if the flows, the alcohol level, or the alcohol temperature fall outside tight limits.

13.3. Gas distribution to the drift volume

At the beginning of Run 2, bubblers with mineral oil were used for both input pressure relief, set at ~5.08 cm (2 in.) H_2O, and for the exhaust, set at ~0.508 cm (0.2 in.) H_20. Assimilation traps with stainless steel wool are placed between the oil bubblers and the rest of the gas system to prevent aerosols from migrating into the lines. Early in Run 2, the input pressure relief bubbler was replaced with a mechanical relief valve utilizing a 30.5 cm (12 in.) diameter diaphragm.

Virtually identical gas lines go to and from the COT drift volume. A 5.08 cm (2 in.) ID stainless steel pipe runs ~45.7 m (150 feet) to the detector and circles the End Wall just outside the 30° crack. Sixteen smaller diameter lines run through the 30° crack. There are four lines in each quadrant, and each line feeds a pair of adjacent superlayers. The lines penetrate the motherboards near the gas seal extrusion, and the flow is split to adjacent superlayers via a tee that penetrates the extrusion. Although the end boards and wedges mostly block the slots in the end plate, the gas flows through the ends of the slots into the drift volume. The drift gas distributes evenly to (and from) the four quadrants.

14. Nitrogen (baggie) purge

When the End Plugs are closed, the volume inside is very isolated. Even small argon / ethane leaks will produce a flammable mixture in a short time without mitigation. The mitigation is done by placing a tent (or baggie) just outside each end plate and flowing nitrogen into the region to inert the entire (non-drift gas) volume between the End Plugs.

The COT leaks are predominately at the motherboards where the ignition sources (high and low voltage) are located. In order to ensure that these areas are properly purged, the purge gas is distributed near the surface of the motherboards, such that there is a uniform flow per unit area of the end plate.

Manifolds with 381 μm (0.015 in.) diameter pinholes spaced by 5.08 cm (2 in.) run along the gas seal extrusions between pairs of superlayers. The manifolds on each end plate are fed by 16 lines (4 per quadrant), and the desired flow through each line is adjusted using variable area flow meters.

The total nitrogen purge flow to each end plate is ~189 l/min (400 SCFH). A 0.635 cm (0.250 in.) diameter Polyflow line with pinholes runs around the surface of the Faraday cage to sample the purge

volume. Gas is pumped from the lines to a sampling box containing a pair of ethane detectors and a pair of oxygen detectors. When running with a 189 l/min (400 SCFH) purge to each end plate, the oxygen level is below 1% and the ethane level is ~9% LEL (Lower Explosive Level of ethane in air). The purge gas eventually leaks out into the Collision Hall through gaps between the cables in the 30° crack.

There cannot be a flammable mixture of argon / ethane (50:50), nitrogen and air if the oxygen level is below 11%. We are far below this value with our normal purge flow, and safety measures are in place to ensure that it never comes close. The nitrogen supply switches over to an auxiliary Dewar if flow decreases significantly from the primary source. Flammable gas flow and power to the CDF detector are automatically shut off if either the baggie purge flow or the baggie sample readings differ significantly from their normal values.

The nitrogen purge also provides a very low humidity environment that is necessary for two reasons. Some of the ASDQ motherboards will draw current at high voltage if the humidity is too high. Also, the silicon detector cooling fluid temperature is normally well below the hall dew point, and the nitrogen purge prevents moisture from condensing on (and dripping from) exposed cooling lines and cooled parts.

15. Data quality monitors: YMon and STAGE0

The quality of the collision data can take unexpected turns for the worse, for example:

- A high voltage daughter board is plugged in offset one wire, not causing a trip, but leaving the supercell dead to real data.
- A flat cable gets pulled loose from a repeater board during a quick access.
- A TDC does not initialize properly at the beginning of a run, such that it detects hits, but with shifted times.

One can envision many more things going wrong, so it is important to continuously run programs which carefully examine collision data.

15.1. YMon

YMon is the name given the first order monitor of detector performance for collision data. A version is always running when data is being taken, and the shift crew scans key plots for abnormalities.

For each COT channel, YMon plots sense wire occupancies, multiplicities, pulse widths, start times and average times. YMon is sensitive not only to readout problems (which are usually well diagnosed by the calibration programs), but also to problems with the high voltage or drift gas.

Since YMon is always running when data is being taken, it is often the first program to catch new problems of any sort. For example, there have been cases where a TDC is left in a badly operating state after initialization at the beginning of a new run. This clearly stands out in the YMon plots of average hit times.

15.2. STAGE0

STAGE0 is both the next stage in monitoring collision data (after YMon) and the initial stage of the offline reconstruction. STAGE0 is a modification of the offline tracking reconstruction program that first optimizes the drift constants using data from that run and then examines various tracking quantities, such as used hits per supercell and average residual per supercell. STAGE0 uses the channel-to-channel t_0 offsets from the calibration database in the same manner as the later offline reconstruction.

ASD cables being swapped between neighboring cells is a good example of a problem that does not show up in the calibration or YMon programs, but generates a large deficit in the plot of used hits in STAGE0. STAGE0 will also track slow changes in drift constants due to problems such as a failure in the temperature regulation of the refrigerator cooling the alcohol bubbler.

The STAGE0 drift constants are fit using a model determined by fitting simulated tracks with drift trajectories predicted by the GARFIELD and MAGBOLTZ [58] programs. A plot of the resulting hit residuals versus drift distance is shown for collision data in figure 31. Figure 32 is a plot of the $KK\pi$ invariant mass distribution in the region of the D^+ and D_s.

16. Cell electrostatics and wire deflections

High voltage is applied to the sense and potential wires to generate a uniform gain and drift electric field for the 30,240 sense wire drift cells. The goal is to create an electric field at the surface of the sense wire of ~180 kV/cm to produce a gain of ~2×10^4 in a uniform drift electric field varying from 1.9 kV/cm for a normal gas (396 ns operation) up to ~2.4 kV/cm for a fast gas (132 ns operation). The drift electric field is chosen to produce a Lorentz angle near 35° for the particular gas mixture.

16.1. Supercell drift field

Figures 33 and 34 show the lines of equal potential and drift trajectories, respectively, for operation with a sense wire surface field of 180 kV/cm, a drift electric field of 2.5 kV/cm, and a Lorentz angle of 35° in argon / ethane / CF_4 (50:35:15). The figures were generated using the GARFIELD and MAGBOLTZ programs.

The sense wires at each end of the supercell have a problem with end effects. In order to contain the drift trajectories and maintain uniform gain, the voltage of the adjacent potential and shaper wires toward the edge of the supercell must be increased significantly. Unfortunately, there is a limit to the voltage difference between neighboring potential wires, which is presently set by the design of the high voltage daughter board. Due to this, the drift trajectories on the end sense wires are not completely optimized.

The effects on drift properties from positive ion distortions have not yet been studied using GARFIELD and MAGBOLTZ. The average affect on the position resolution is ~1% that of the CTC at the same luminosity due to the much smaller drift distance and higher drift electric field of the COT. Since we did not see any appreciable affects with the CTC in Run 1, the COT should be in good shape for Run 2 with instantaneous luminosities about an order of magnitude higher.

16.2. Wire motion due to electrostatic forces

An unfortunate side affect of creating the drift field is to produce electrostatic forces on the wires and field planes, causing them to move. As the electric field is increased, the COT first becomes sensitive to the sense and potential wires stepping out of plane and then to the coherent forces on the wire plane as a unit.

The critical wire tension below which the cell becomes unstable, T_c, was estimated for the wire stepping when operating at the design maximum field of 2.5 kV/cm. Without the pultrusion rod center support, $T_c \approx 150$ g, and this value is reduced to 43 g with the center support. In practice the wire tension should be far above T_c, since large wire motions precede the instability. By using the center support and 150 g wire tension, the differential motion of wires within the plane reaches a maximum of less than 25.4 μm (0.001 in.), one quarter of the way along the wire from the end plate at 1.9 kV/cm.

The coherent motion of the wire plane was studied using field sheets with and without a center support. The wire plane will not move if it is perfectly centered between the field sheets, but a "bias" toward either plane will cause both the wire plane and field sheets to move. The ratio of the wire plane motion to bias, "K-1", was measured as a function of the drift field, and the results are shown in figure 35.

Data was taken using field sheets with and without a center support. The curves are fits to a model that describes the electrostatic motion. By using center supports, the field where K-1 increases rapidly toward instability is increased by ~3 kV/cm. One clearly wants to operate in a region where K-1 is less than 1, so the field plane center supports were added to give more flexibility in operating point when running with a fast gas.

16.3. Additional electrostatics problem with stereo superlayers

The stereo supercells have an additional positioning problem with the field sheets due to the twist angle generated in the sheet by stepping 6 supercells in ϕ as it runs between end plates. The twist angle varies from 13° in superlayer 1 to 5° in superlayer 7. Unless one perfectly positions the angle of the end board with respect to the end plate, the resulting inequality of diagonal forces across the length of the sheet will result in an additional sag in the sheet, which in turns causes a deflection of the

wire plane when the drift field is increased. At 2.4 kV/cm, the deflection in superlayer 1 is ~25.4 μm (0.001 in.) if the angle of the end board is off by 25.4 μm (0.001 in.) over the 11.4 cm (4.5 in.) length of the end board ledge (the affect on SL7 is less by the ratio of the twist angles). The scaling with drift field follows figure 35.

We could not control the angle of the ledge to end plate at the 25.4 μm (0.001 in.) level, and measuring the position of the planes using capacitance (as in section 4.2) was impractical during the chamber stringing because the field sheets could not easily be isolated from the end plate ground. Instead, a ledge was used that only contacts the end plate near its center. As described in section 5.5, during the final seating a pulley system was used to momentarily pull back the end boards and allow the tensions to equalize.

Each supercell was then tested at an elevated electric field that was just shy of the typical point of instability (about 2.8 kV/cm, see figure 35). A small number of cells (less than 1%) failed the test, and most of the failures were fixed by repeating the seating procedure. The other failures were due to defects with either the field or wire planes, and the bad planes were either repaired or replaced. This procedure ensures that there are no large biases due to the stereo twist, but we may not know the wire position as accurately as desired at large drift fields. This argues for operating at as low a drift field as practical for the particular drift gas, and measuring the change in wire position with tracks as the field is increased.

16.4. ϕ-dependent wire position: gravitational and electrostatic forces.

A combination of electrostatic and gravitational forces determines the position of the wire. The calculated gravitational sag of the wire is given by

$$y(\mu m)=[-203.5\ (1-(z/(L/2))^2)]-[59.4\ (1-|z|/(L/2))]\ ,$$

where L = 310 cm is the wire length. Figure 36 shows this quantity as a function of |z|. The first term within square brackets is due to the weight of the wire and the second is due to the center support. The equation was derived using the median linear density of the wire (0.253 mg/cm, which can vary by ± 3% from spool to spool) and the nominal tenision (150 g, which can vary by ± 5%). The measured tension and linear density of each wire is stored in a database that can be used to determine the wire position in the track reconstruction program.

Figure 37 shows the motion of the wires at the center of the chamber in z as a function of ϕ when the drift field, E, is raised from 0 to 2.4 kV/cm. The motion is perpendicular to the plane of wires and is measured with respect to the same field sheet as the cell is rotated in ϕ. The direction of motion is up (opposite the sag) at ϕ(fig. 37) = 0° and 180°, where the field sheet is horizontal with the stainless steel wires above and below the sheet, respectively. Note that ϕ(CDF) = ϕ(fig. 37) + 145°, where ϕ(CDF) is defined in the standard CDF coordinate system. The measurements were made using production wire planes and field sheets in the pre-production prototype. The amplitude of the sinusoidal (in ϕ) electrostatic motion is 117 μm (0.0046 in.), and there is an average shift toward one field sheet of 84 μm (0.0033 in.). Both quantities decrease by a factor of 2.7 at E = 1.9 kV/cm, as indicated in figure 35.

Table 5 lists the y and x offsets at z = 0 relative to z (end plate) for E = 2.4 kV/cm and 1.9 kV/cm for the cases where the wire plane is either horizontal or vertical. Since the electrostatic deflection and the uncertainty in wire position it introduces increases significantly with drift field, it is best to run at as low a field as the drift properties will allow for a given gas mixture.

17. Wire aging studies and the Gas Monitor Chambers

Wire aging is always a concern when operating a drift chamber in a high radiation environment for long periods. When describing the gas system in section 13, many components were motivated by their usefulness in reducing aging seen either by the CTC or test chambers during Run 1. One of the most important lessons learned in Run 1 was to continuously monitor wire aging in test chambers placed at several places throughout the gas system. For Run 2 these chambers are called Gas (or Aging) Monitor Chambers (GMCs), which are described in section 17.2. Section 17.1 describes aging tests

performed specifically for operation of the COT in Run 2.

17.1. Aging tests for the COT in Run 2.

Aging tests for the COT had to begin early in the project in order to influence the design. At that time, the Run 2 integrated luminosity was thought to be 2 fb^{-1}, so tests stopped short of what one would do given the present projections.

At the time of writing, it appears that the integrated luminosity will likely fall between 2 fb^{-1} and 8 fb^{-1}, and it is not clear what fraction of the running will be done with 132 ns bunch spacing. Our best estimate of the maximum wire current for Run 2 is that for superlayer 1: 4.5 μA/wire (15 nA/cm) at 2×10^{32} $cm^{-2}s^{-1}$. The integrated charge on a superlayer 1 sense wire will fall between 0.15 C/cm and 0.60 C/cm.

We began the tests with a similar gas mixture as was used for the CTC, argon / ethane (50:50) + alcohol, and substituted CF_4 for ethane to create a faster gas for running at 132 ns bunch spacing. Aging tests were performed with chambers built with the same materials used to construct the COT, and the supercell configuration was essentially the same except that it was not tapered (see GMC design in figure 38). The more precise tests were conducted at constant pressure and over a very small temperature range.

Table 6 lists the results of bench top aging measurements for both normal and fast gases using an Sr^{90} source. The tests were performed at constant pressure over a small temperature range using primary grade gas mixtures from Airgas Corporation [59]. The gain variation with temperature was carefully mapped out and the data appropriately corrected. These tests were performed with a somewhat smaller isopropyl alcohol content than we are presently using, but all of our bench tests showed a decrease in aging rate with small increases in the alcohol content.

The gain loss with isopropyl alcohol and no CF_4, 5% CF_4 and 15% CF_4 are all less than ~1% for an integrated charge of 1 C/cm. Without the addition of alcohol, the gain decrease in argon / ethane (50:50) was 19.3% /C/cm. Including systematic effects, the estimated uncertainty in the measurements is 2% /C/cm. No significant change in aging rate was observed between wire currents of 30 nA/cm and 290 nA/cm.

The resistivity (ohms/square) of the gold / Mylar field sheet was also monitored. No change was seen up to 0.63 C/cm, which was the maximum charge accumulated during each test. Based on these bench measurements, we decided to use argon / ethane (50:50) + isopropyl alcohol when operating with a 396 ns bunch spacing and argon / ethane / CF_4 (50:35:15) + isopropyl alcohol when operating with a 132 ns bunch spacing.

17.2. Gas Monitor Chambers

A schematic of a GMC [57] is shown in figure 38. Each chamber contains four supercells: two near the Sr^{90} source (1 and 2) and two far from the source (3 and 4). Since the chambers are placed at remote locations in the gas system, they were designed to provide an accurate aging measurement with no local interaction (such as substituting an Fe^{55} source for the Sr^{90} source, as was done in Run 1). The accuracy is obtained by using ratios of currents of the three cells nearer the source to that of the farthest cell, cell 4. R1 is the ratio of the current in cell 1 to that in cell 4, and R2 and R3 are similarly defined. The ratios are quite insensitive to changes in temperature, pressure, high voltage supply calibration, and gas composition.

The four supercells are operated with the same high voltage power supplies at a gain and drift electric field close to that of the COT. The effective current density at the wires is approximately 100 nA/cm, 60 nA/cm, 15 nA/cm and 10 nA/cm for cells 1 – 4, respectively. When doing aging measurements using the ratios R1 and R3, the difference in current densities of cells 1 and 3 relative to cell 4 correspond to COT superlayer 1 operation at luminosities of ~10^{33} $cm^{-2}s^{-1}$ and ~10^{32} $cm^{-2}s^{-1}$, respectively. Therefore, one has an aging measurement at current densities far above those expected in Run 2 to locate problems before they affect the COT and a measurement at typical Run 2 values.

The ratios are still slightly dependent on gas density (temperature and pressure) due to the larger space charge density effects in the planes near the source. By once measuring the change in the ratios as the gain is varied, one can correct all future

measurements back to effectively the same gain. Figure 39 shows the results of a typical aging measurement, displaying the time dependence of R1 before and after the space charge density correction.

GMC aging measurements are being made continuously during Run 2. GMC 1 is located at the input to the COT (at the circular manifold before the 16 lines pass through the 30° crack), GMC 2 is located at the exhaust of the COT (at the manifold just after the lines pass through the 30° crack), and GMC 3 is located just after the alcohol bubbler on the gas platform. In typical measurements spanning 3 to 4 weeks, the ratios R1, R2 and R3 of all chambers show gain drops of less than 2% /C/cm, and we estimate that the present systematic error in the measurements is 5% /C/cm. Therefore, at this time there are no indications that the COT is in danger of significant aging.

18. Summary

We have described the design, construction and operation of the Central Outer Tracker, the central drift chamber for the upgraded CDF detector in Run 2. Like its predecessor, the CTC, the COT is an open cell design with superlayers and supercells, but the maximum drift distance is a factor of four smaller and there are twice as many measurements in the stereo superlayers. The Can, the support structure for the wire planes and field sheets that create the supercells, consists of two annular aluminum end plates connected by an aluminum outer cylinder and a carbon fiber / epoxy composite inner cylinder. The wire planes and field sheets are mounted in narrow slots in the end plates, and precise features on their end boards are mated to precise features in the slots.

Each wire plane contains 12 sense wires, 13 potential wires, and 4 shaper wires, and all wires are tungsten with gold plating. Before installation into the Can, the planes were tested for wire position within the plane, wire tension, plane length at nominal tension, and integrity at high voltage with sources. The field sheet consists of extremely thin gold / Mylar material with stainless steel edge wires to carry the bulk of the load. Before installation, the sheets were tested for overall shape, ripples, and length at nominal load. Both the field sheet and wire plane have a center support rod that limits motion due to electrostatic forces.

After the Can was pre-tensioned to simulate the final load, stringing engines were used to install the wire planes and field sheets at controlled tension. The engines, along with automatic rotational indexing of the Can, allowed the installation of ~60 supercells each day. The wire tensions were checked daily during the stringing process and again after completion.

Aluminum gas seal extrusions were installed in shallow grooves between superlayers in the end plate, and motherboards were connected to the pins on the wire plane end boards. The borders of the motherboards to both their neighbors and the extrusions were epoxied to create a gas seal that surpassed our specifications. The motherboards feed through the sense and potential wire connections to daughter boards that contain the ASDQ readout chips on one end and distribute high voltage on the other.

The high voltage system uses VME based BiRa power supplies and has external filter and crowbar circuits. The ASDQ chip allows operation at low threshold (close to 2 fC), has effective baseline restoration, and generates an LVDS output pulse width that is logarithmically proportional to the input charge. Filtered power (with sensitive over current protection) and isolated control voltages are distributed to the ASDQ daughter boards in separately controllable units of superlayer / quadrant.

Following the ASDQ, the readout consists of micro-coax cables through the limited space in the 30° crack, repeater boards mounted on the End Wall Calorimeter, flat cables with copper mesh backing that make the long run to the corners of the End Wall, and TDC boards housed in VME crates. From the TDC, fast signals are sent to the XFT to produce a track trigger at Level 1, and digitized signals are sent through the remainder of the readout chain.

A calibration network is used to measure the relative t_0 of all channels to an accuracy of 0.5 ns. The YMon program monitors chamber performance during the data taking. The STAGE0 program provides updated drift constants for each run and monitors the track reconstruction performance. In the early data taking and analysis, the hit residuals and resonance mass resolutions are close to expectations.

The system for delivering the drift gas (presently argon / ethane (50:50) + isopropyl alcohol) was constructed with concerns about wire aging in mind. The SUVA cooling system, the SVX insulation and heaters, and the TOF heaters keep the COT Can reasonably close to its assembly temperature, and the SUVA effectively cools the ASDQ chips. The nitrogen (baggie) purge keeps the region inside the End Plugs far below flammable limits and provides the dry atmosphere necessary to operate the COT high voltage and SVX cooling.

The supercell's lines of equal potential and drift trajectories were studied using the GARFIELD and MAGBOLTZ programs. The effect of electrostatic forces on wire position at high drift fields were measured and are significant, but manageable. Gas Monitor Chambers are placed at three locations in the drift gas system, and to date their aging rates are low, as expected from bench tests.

Acknowledgments

The authors thank the Fermilab staff and the technical staffs of the participating institutions for their vital contributions. This work was supported by the U.S. Department of Energy, the U.S. National Science Foundation and the Alfred P. Sloan Foundation.

References

[1] F. Bedeschi et al., "Design and Construction of the CDF Central Tracking Chamber" NIM A268 (1988) 50-74.
[2] R. Blair et al., "The CDF II Detector Technical Design Report", Fermilab-Pub-96/390-E (1996).
[3] K. Burkett, "Design and Construction of the CDF Central Outer Tracker", Pub. Proceedings 8th Pisa Meeting on Advanced Detectors, La Biodola, Isola d'Elba, May 21-27, 2000.
[4] http://www1.dupont.com/NASApp/dupontglobal/corp/index.jsp
[5] Brenner Tool and Die, Inc., 921 Cedar Ave., Croydon, PA 19021 USA
[6] Pierce Aluminum Co., Inc., 136 Will Drive, Carton, MA, 02021-0100 USA
[7] STADCO (Standard Tool and Die Company, division) 1931 N. Broadway, Los Angeles, CA 90031 USA
[8] http://www.3m.com/
[9] Advanced Composites, Inc., 1154 South 300 West, Salt Lake City, Utah 84101 USA
[10] http://www.toray.co.jp/
[11] http://www.dow.com/Homepage/index.html
[12] http://www.airproducts.com/
[13] http://www.hysol.com/
[14] Osram Sylvania Inc., Chemical and Metallurgical Products, Hawes Street, Towanda, PA 18848-0504 USA
[15] VECTRA Customer Service - USA, Celanese Specialty Operations, 86 Morris Avenue, Summit, NJ 07901 USA
[16] http://www.hexcel.com/
[17] http://www.gcwaldom.com/
[18] http://www.imtrongmbh.de/lab-windows/
[19] Sheldahl, 1150 Sheldahl Road, Northfield, MN 55057-9444 USA
[20] Major Wire, Inc., 7014 West Cullom Avenue, Chicago, IL 60634 USA
[21] Shell Oil Company, P.O. Box 4320, Houston, TX 77210 USA
[22] http://www.cabot-corp.com/
[23] http://www.slosyn.com/
[24] http://www.leespring.co.uk/
[25] http://www.savacable.com/
[26] http://www.ni.com/
[27] http://www.hypertronics.com/
[28] http://www.conformal-coating.com/parylene_coating.htm
[29] Bower Manufacturing Co., 6565 Sprinkle Road Kalamazoo, MI 49001-8705 USA
[30] http://www.emersoncuming.com/
[31] http://www.acehardware.com/
[32] BiRa Systems, Inc., 2404 Commanche NE, Alburquerque, NM 87107 USA
[33] http://microsoft.com/
[34] SBS Bit3, 1284 Corporate Center Drive, St. Paul, MN 55121-1245 USA
[35] VMIC, 12090 South Memorial Parkway, Huntsville, AL 35803-3308 USA
[36] http://www.intellution.com/
[37] http://www.eupec.com/
[38] http://www.vishay.com/brands/dale/resistors.html
[39] http://www.xicon-passive.com/
[40] W. M. Bokhari et al., "The ASDQ ASIC", IEEE Trans. On Nucl.Sci., 43 (June, 1996) p 1725.
[41] R. Veenhof, "A drift-chamber simulation program, User's guide", CERN, Version 5.05 (1994).
[42] MAXIM Integrated Products, Inc., 14320 W. Jenkins Road, Beaverton, OR 97005 USA
[43] http://www.subtronics.com/
[44] http://www.vicr.com/
[45] http://www.analog.com/
[46] http://www.omroncomponents.co.uk/Relays.htm
[47] http://www.habia.se/
[48] Bay Associates, Inc., 150 Jefferson Drive, Menlo Park, CA 94025 USA
[49] http://www.intersil.com/cda/home/
[50] http://www.amphenol.com/

[51] E. J. Thomson et al., "Online Track Processor for the CDF Upgrade", IEEE Transactions on Nuclear Science, Vol. 49, No. 3, June 2002.
[52] http://www.berkeleynucleonics.com/cinfo.htm
[53] http://www.timesmicrowave.com/
[54] http://www.motorola.com/
[55] http://www.suva.dupont.ca/suva410a.htm
[56] http://www.kscorp.com/www/index.html
[57] M. Binkley et al., "Aging in Large CDF Tracking Chambers", Proceedings International Workshop on Aging Phenonmena in Gaseous Detectors, DESY, Hamburg, Germany (2001); FERMILAB-CONF-02/041-E.
[58] S. F. Biagi, MAGBOLTZ computer code, see also consult.cern.ch/writeup/magboltz/
[59] http://www.airgas.com/

Table 1: Comparison of CTC and COT. For both the CTC and COT, all tungsten (W) wires, including all sense wires, have a diameter of 40 μm and are gold plated. The diameter of the stainless steel (SS) wires in the CTC varies from 140 μm (0.0055 in.) to 305 μm (0.012 in.), and the diameter of the SS wires epoxied to the gold / Mylar sheet in the COT is 305 μm (0.012 in.).

	CTC	COT (396 ns spacing)	COT (132 ns spacing)
Gas	Ar/Et (50:50)+Ethyl	Ar/Et (50:50)+Isopropyl	Ar/Et/CF_4 (50:35:15)+Iso
Max. Drift Dist., Time[a]	3.6 cm, 706 ns	0.88 cm, 177 ns	0.88 cm, 100 ns
Lorentz Angle	~45° (45° cell tilt)	~31° (35° cell tilt)	~42° - ~35°
Drift Field	1.25 - 1.35 kV/cm	1.9 kV/cm	2.1 - 2.4 kV/cm
Radiation Lengths	1.7%	1.7%	
Total Layers	84 [in 9 superlayers (SL)]	96 (in 8 SL)	
Layers/SL	12-6-12-6-12-6-12-6-12	12-12-12-12-12-12-12-12	
Stereo Angle	± 3°	± 2°	
Total Sense Wires (SW)	6156	30,240	
SW tension, spacing, len.	135g, 7.620 mm, 310 cm	150g, 7.112 mm, 310 cm	
Total Wires	6156 W + 30,348 SS	73,080 W + 5040 SS	
Cathode design	SS wire plane	Gold / Mylar sheet (2 SS)	
End Plate Load	~25,000 kg	36,132 kg	

[a]Typical at center of superlayer

Table 2. COT superlayers

SL	Stereo Angle (°)	# cells	<r> (cm)
1	+2	168	46.774
2	0	192	58.534
3	-2	240	70.295
4	0	288	82.055
5	+2	336	93.815
6	0	384	105.575
7	-2	432	117.335
8	0	480	129.096

Table 3. Radiation lengths in the COT active volume. <L> is obtained from the Cell density by multiplying by the number of cells (2520) and dividing by the average radius (553 cm).

Component	**Cell density (g/cm)**	**X_0 (g/cm^2)**	**$<L>/X_0$ (%)**
Field Sheet			**0.628**
Mylar (1.39g/cm^3)	.00874	39.95	0.100
Gold (19.32 g/cm^3)	.00134	6.44	0.095
SS wire	.0111	13.84	0.365
Center support	.0022	27	0.037
Epoxy	.0027	40	0.031
Wire Plane			**0.524**
Tungsten (19.30 g/cm^3)	.00703	6.76	.474
Gold (5%)	.000352	6.44	.025
Center support	.00107	~19.4	.025
	Length (cm)	**X_0 (cm)**	**$<L>/X_0$ (%)**
Gas			**0.557**
argon (50%)	92.49 cm	10983	0.421
ethane (50%)	92.49 cm	34035	0.136
Total			**1.709**

Table 4. ASDQ Specifications

Quantity	Specification
Technology	Rad-Hard Anal. Bipolar
Channels	8
Package / Pins	Quad flat pack / 64
Power (stability)	±3V DC (±5%)
Power dissipation	40 mW per channel
Channel crosstalk	< 1%
Thres. Temp. Sensitivity	0.1 fC / 10°C
Input imped. (Low freq.)	260Ω (Total: 300Ω)
Input imped. (High freq.)	30% roll-off at ~30 MHz
Noise (10 pF input cap.)	~ 2300 electrons

Table 5. The offset in y and x at z = 0 with respect to z (end plate) for the cases where the wire plane is horizontal (145 and 325°) and vertical (235 and 55°). The first value is for E = 2.4 kV/cm and the second (inside parentheses) is for E = 1.9 kV/cm.

ϕ (CDF) (Degrees)	Δy (el) (μm)	Δy (el+gr) (μm)	Δx (el) (μm)
145	201 (74)	-62 (-189)	0
235	0	-263	-84 (-30)
325	33 (13)	-230 (-250)	0
55	0	-263	84 (30)

Table 6. Aging with various gas mixtures.

Gas Mixture	ΔG/G per C/cm
ar/ethane/CF_4(50:35:15)+Iso[a]	(0.9±0.4)%
ar/ethane/CF_4(50:45:5)+Iso	Same as above
ar/ethane(50:50)+Iso	(-0.7±0.3)%
ar/ethane(50:50)	(-19.3±0.6)%

[a]Flow gas through isopropyl alcohol at -4°C

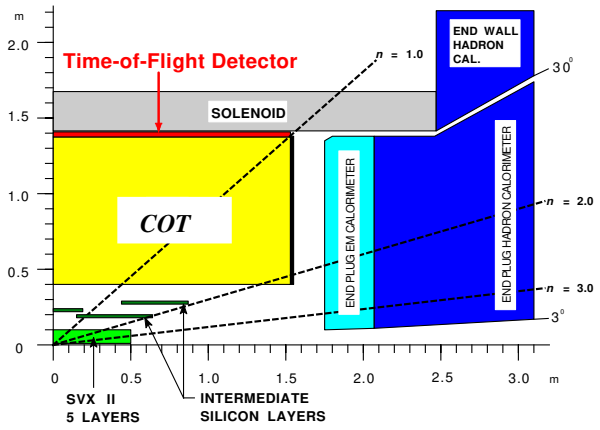

Figure 1. Side view of the central region of the CDF detector (quarter section), showing the location of the COT.

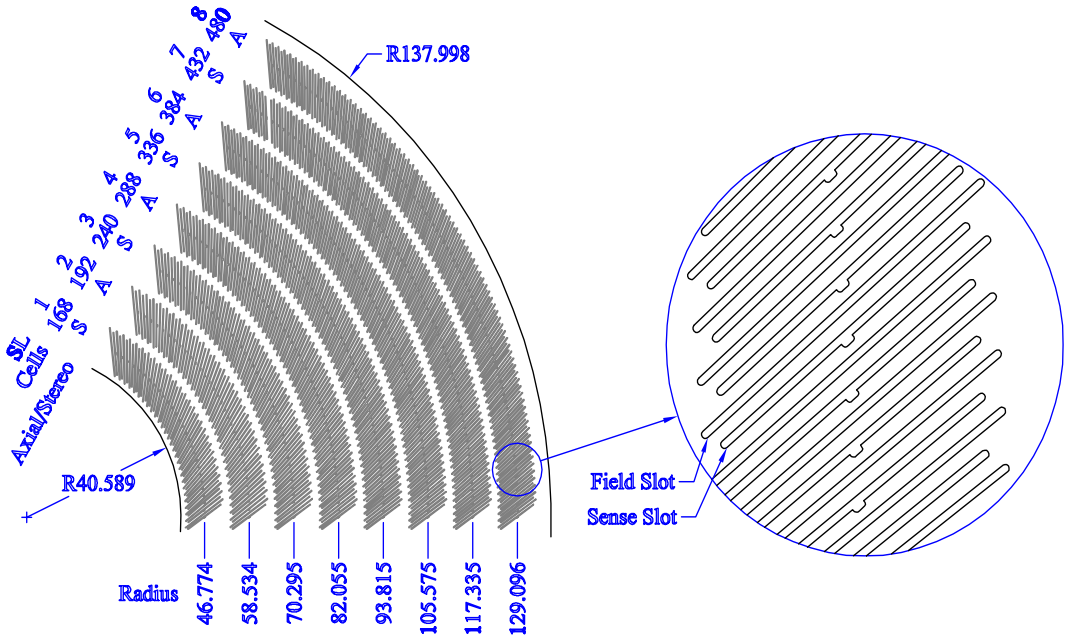

Figure 2. 1/6 section of the COT end plate. For each superlayer is given the total number of supercells, the wire orientation (axial or stereo), and the average radius. The enlargement shows the sense and field slot geometry in detail. Dimensions are in cm.

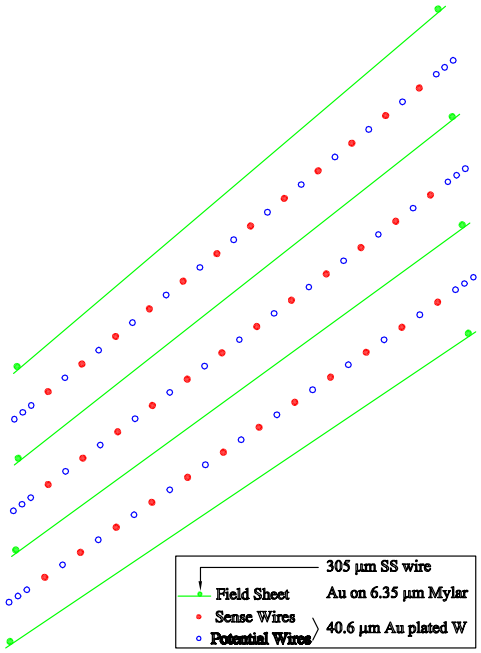

Figure 3. Three supercells in superlayer 2 looking along the beam (z) direction. Some details in this sketch are not precise, such as the position of the shaper wires.

Figure 4. The COT during "stringing" of the wire planes and field sheets. The carbon composite inner cylinder, aluminum end plate (east) and aluminum outer cylinder are visible. Superlayers 1-5 have been strung and superlayer 6 is about half done. A wire plane is being inserted at 10:00 and a field plane at 4:00. Pre-tension fixtures are seen in superlayers 6 – 8.

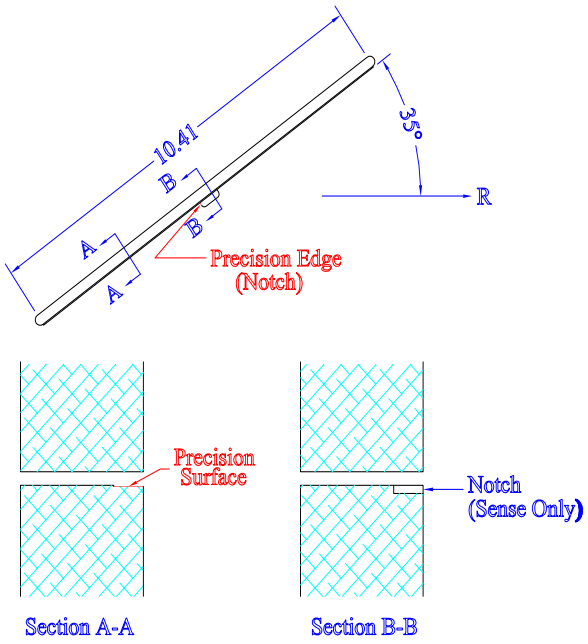

Figure 5. A sense slot in the end plate in the r-ϕ (top) and r-z (Sections A-A and B-B) views. A field slot has the same geometry, except that there is no Notch and the length is 11.94 cm. The machining tolerance on the Precision Notch Edge is ± 38.1 μm (0.0015 in.) and that on the Precision Surface is ± 50.8 μm (0.002 in.) for the sense slot and ±76.2 μm (0.003 in.) for the field slot. The Precision Surface extends 0.762 cm (0.300 in.) from the gas side of the end plate.

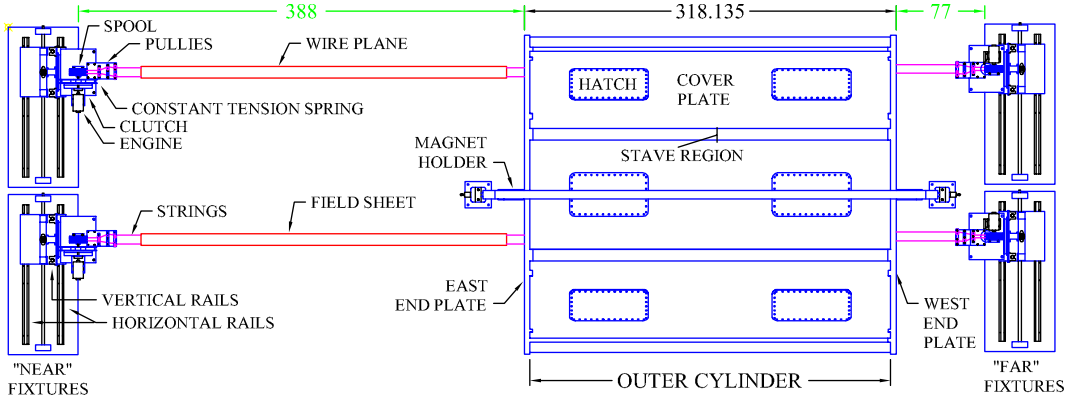

Figure 6. An overhead view of the COT Can in position for stringing the wire planes and field sheets. Components of the outer cylinder are labeled and the nominal distance between the outside surfaces of the end plates is indicated. Figure 7 details a region where the cover plate and stave are screwed to the end plate. Dimensions are in cm.

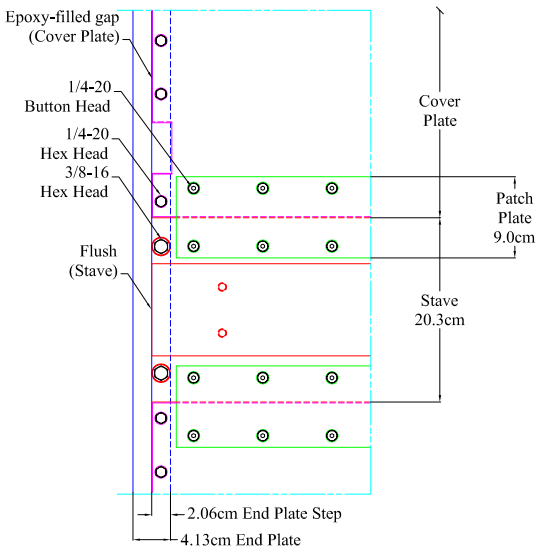

Figure 7. A portion of the outer cylinder near the end plate.

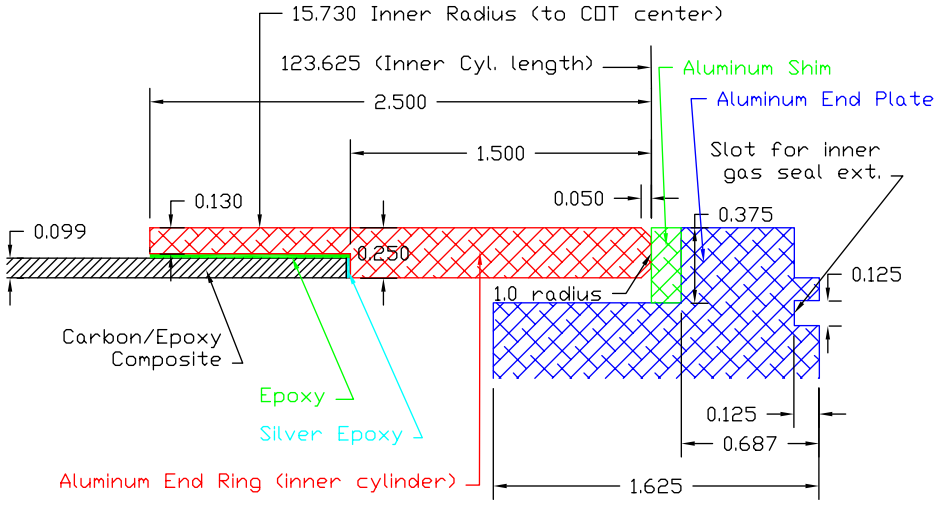

Figure 8. The inner cylinder at the point where it contacts the shim and end plate. Not shown is the 0.001 in. (25.4 μm) thick aluminum sheet that is epoxied to the outer surface of the cylinder. Dimensions are in inches (2.54 cm).

Figure 9. Alignment Fixture with the end plates, inner cylinder, and partial outer cylinder (reinforced staves, and two cover plates). Some pre-string lines are installed.

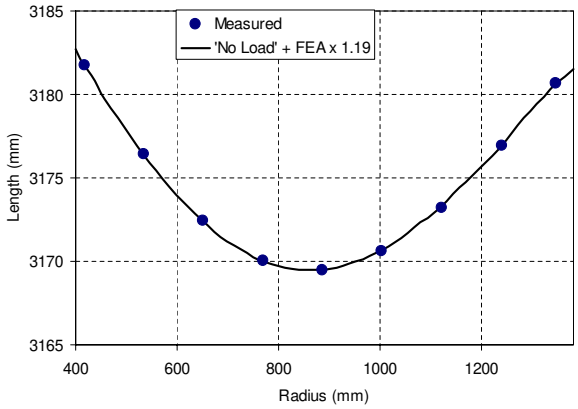

Figure 10. The length of the COT (distance between the outside surfaces of the two end plates) as a function of radius after the load is applied. The FEA prediction of the deflection was scaled by 1.19 to match the measurements.

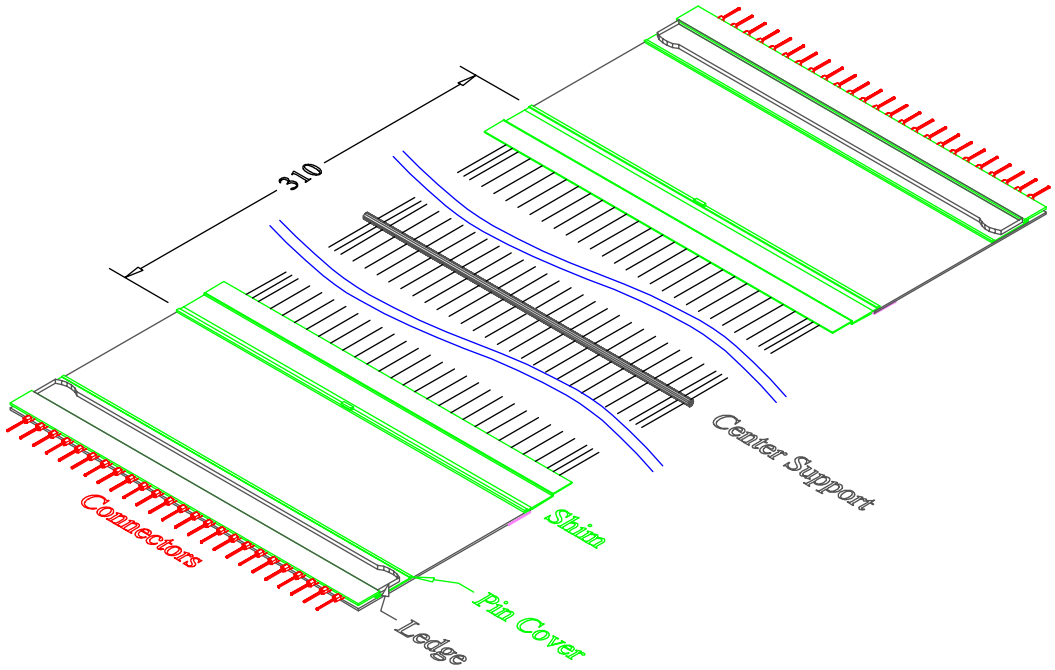

Figure 11. An isometric view of the wire (sense) plane. When installed into the Can, the bumps on the Ledge contact the atmosphere side of the end plate, and precise features of the Shim (figure 13) contact precise features of the Slot (figure 5). Some details in this sketch are not precise, such as the position of the shaper wires.

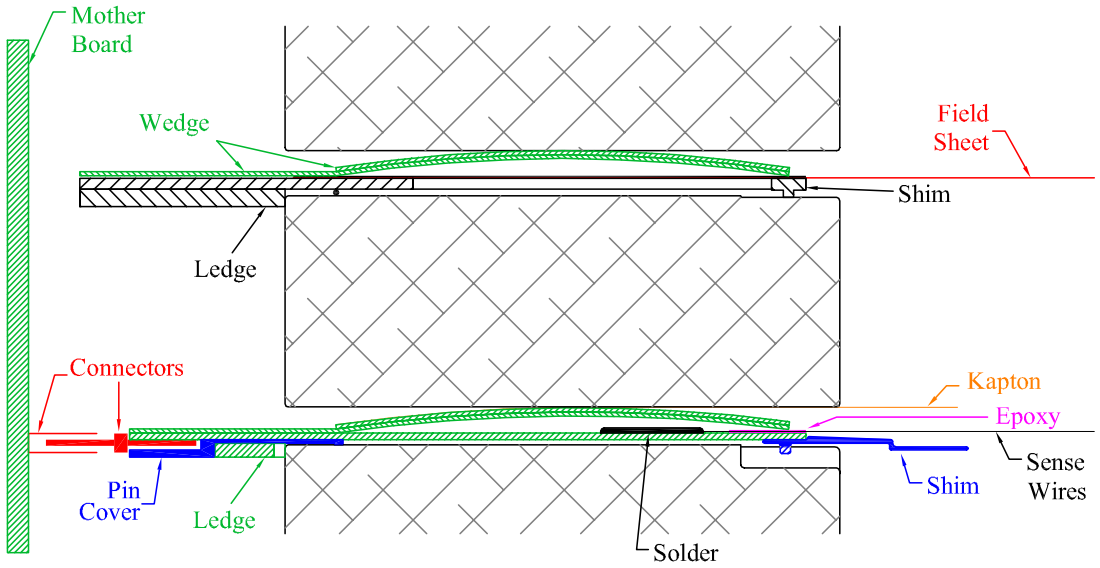

Figure 12. A section through the center of the long dimension of the end plate slots (section B-B in figure 5) showing a wire (sense) plane and field sheet after installation. At the center, the notch occurs in the precise surface of the wire plane slot, the arc in the field sheet end board is at its maximum extent, and the wire plane (field sheet) ledge does not (does) make contact with the end plate. Details of the wire plane, field sheet, and installation procedure can be found in sections 3, 4 and 5, respectively. The G10 wedge is described in section 3.

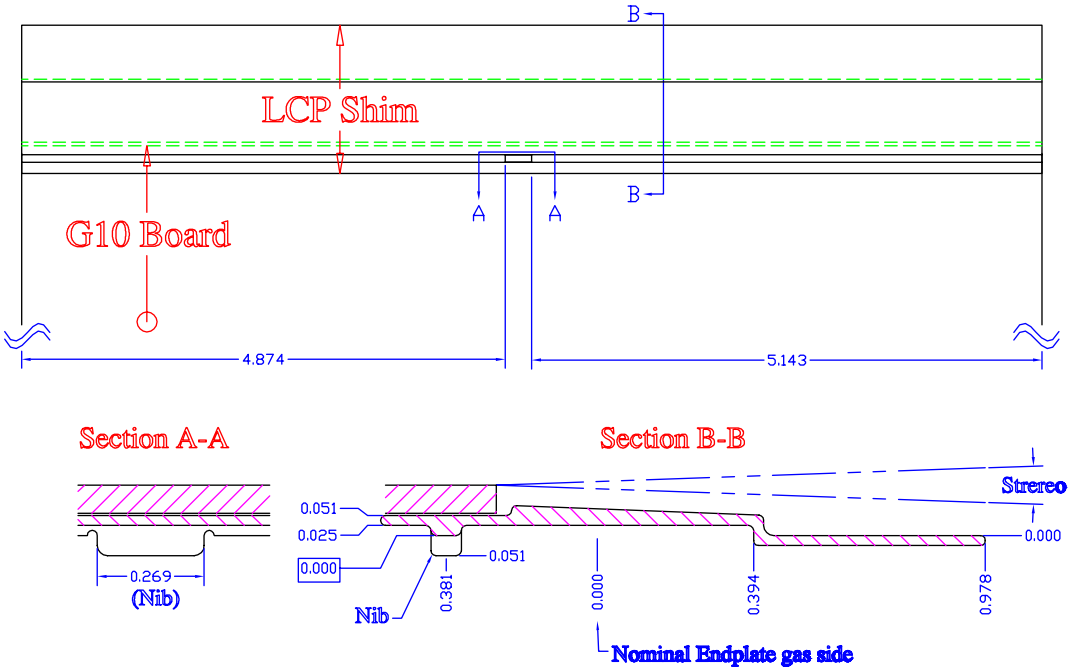

Figure 13. The wire plane LCP shim attached to the G10 end board. One of the nib edges (vertical in Section A-A) seats against the precise edge of the end plate notch, and the bottom ridge (apart from the nib) in Section A-A seats against the precise surface of the end plate slot (0.000 cm). The dashed lines indicate the possible paths of wires in stereo superlayers. The wire centers are 0.1389 ± 0.0013 cm (0.0547 ± 0.0005 in.) above the precise slot surface at the edge of the G10 board (the release point from the epoxy strip, which is not shown). All dimensions are in cm.

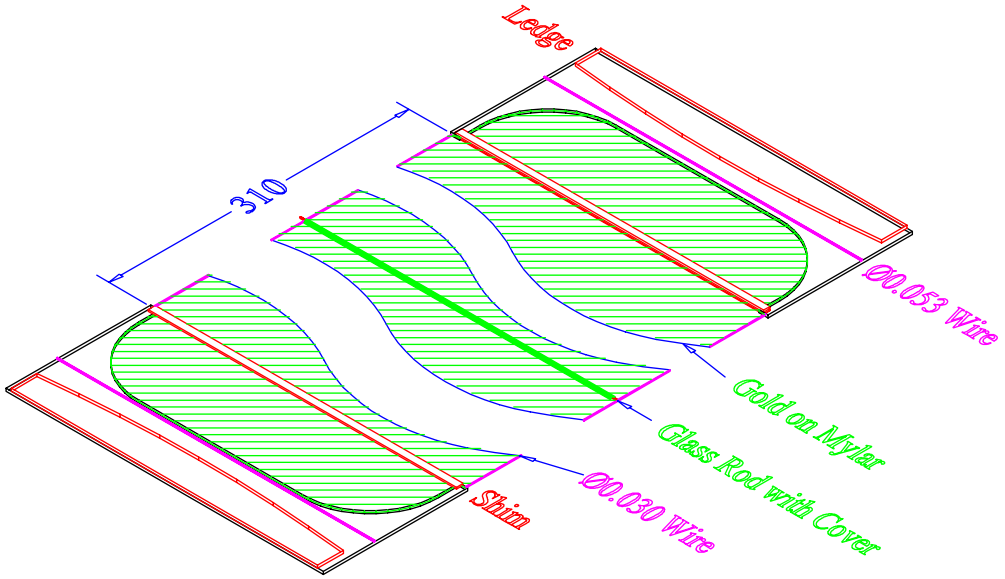

Figure 14. Isometric view of the field sheet. The 0.053 cm diameter wire parallel to the precise shim is the “back shim” described in section 3.1 and also shown in figure 12 . Dimensions are in cm.

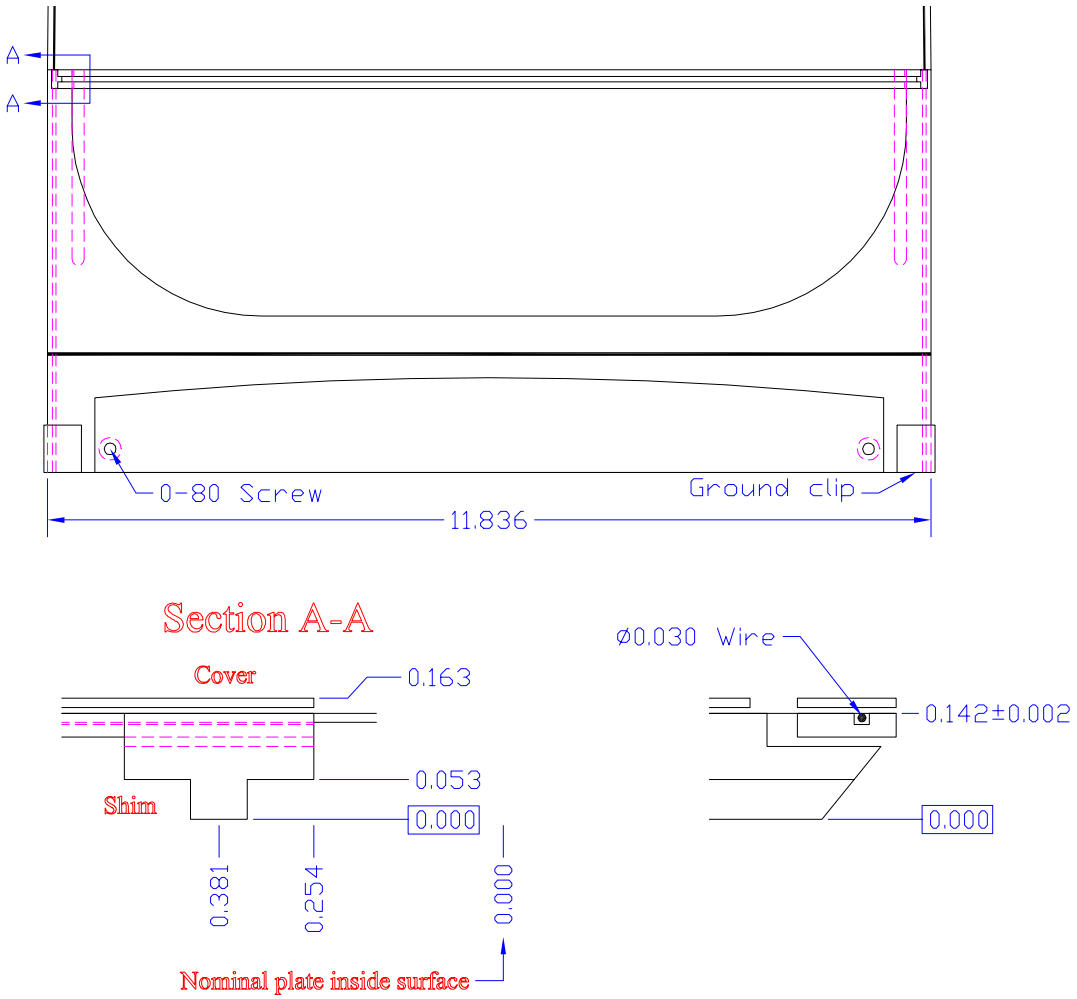

Figure 15. Drawing of the field sheet in the region of the end board. The top portion shows the ledge attached with 0-80 screws and the ground clips that reference both the wires and gold / Mylar to the end plate ground. Section A-A shows the relationship between the gold / Mylar (at 0.142 cm) and the wire (inside a groove in the main end board) to the field shim, which seats against the precise surface of the end plate slot along the bottom edge (0.000 cm). The above are design dimensions. The "as built" distance of the gold / Mylar above the precise surface is 0.152 ± .005 cm. Dimensions are in cm.

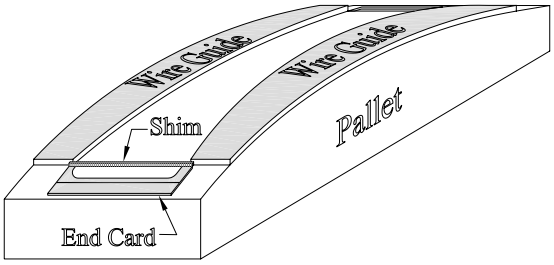

Figure 16. A sketch of the fixture used to assemble the field sheets. The arcs of the pallet and wire guides are exaggerated.

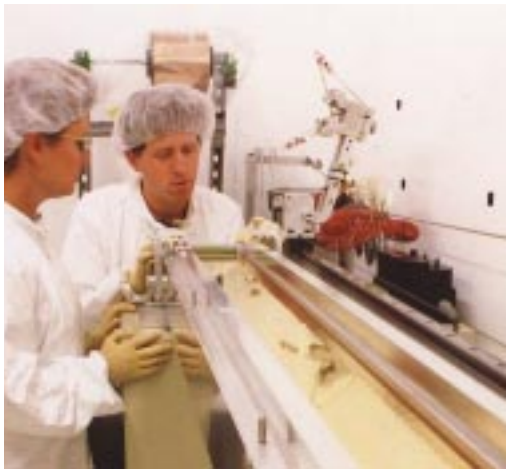

Figure 17. Technicians adjusting the position of an end card before rotating the arm of the epoxy applicator so that the syringe tips ride along the stainless steel wires. The wire guides are in place over the gold / Mylar sheet, which was unrolled from the spool in the background.

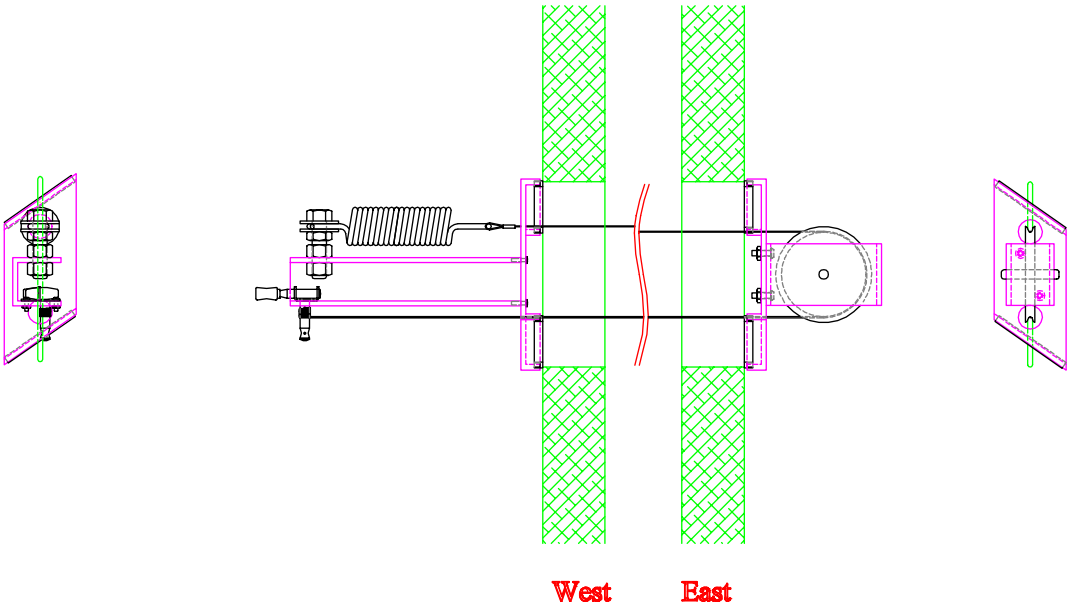

Figure 18. Fixture used to pre-tension the Can before installing the wire planes and field sheets.

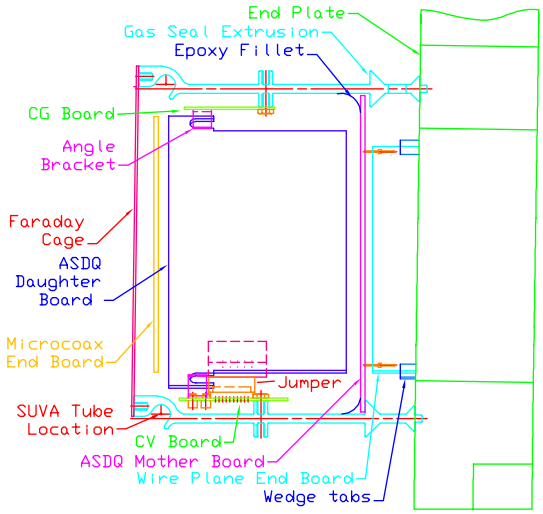

Figure 19. Side view of the gas seal and readout components. With the exception of the Faraday Cage, the components are rectilinearly related to the x-y plane and not the loaded End Plate, shown here at SL8.

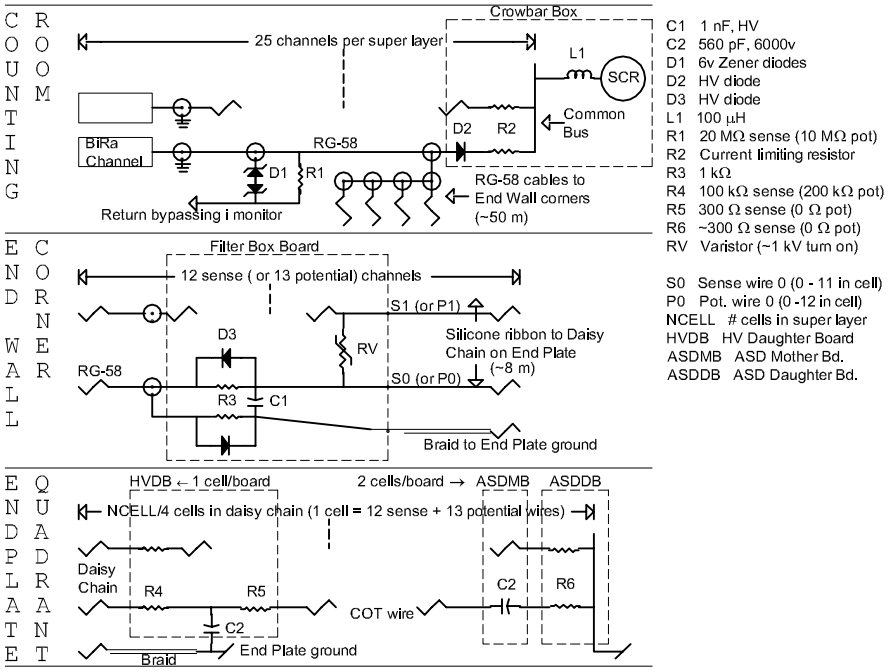

Figure 20. The distribution of high voltage for one superlayer. The figure is divided into sections corresponding to components located in the Counting Room (first floor), on each corner of the End Wall [East (West) End Wall for superlayers 2, 3, 6, 7 (1, 4, 5, 8)], and on the COT End Plate.

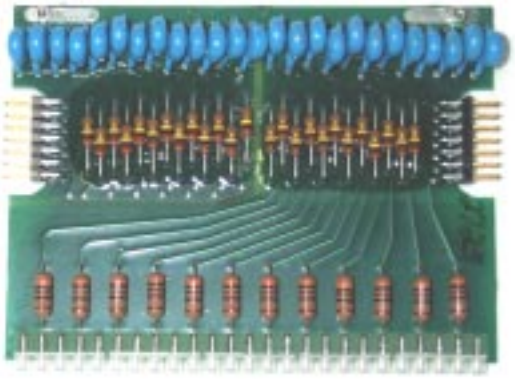

Figure 21. The high voltage daughter board. From bottom to top are the sockets with funnels, 300 Ω resistors (sense wires), 100 kΩ and 200 kΩ resistors to headers for silicone ribbon cable connection, and 560 pF capacitors.

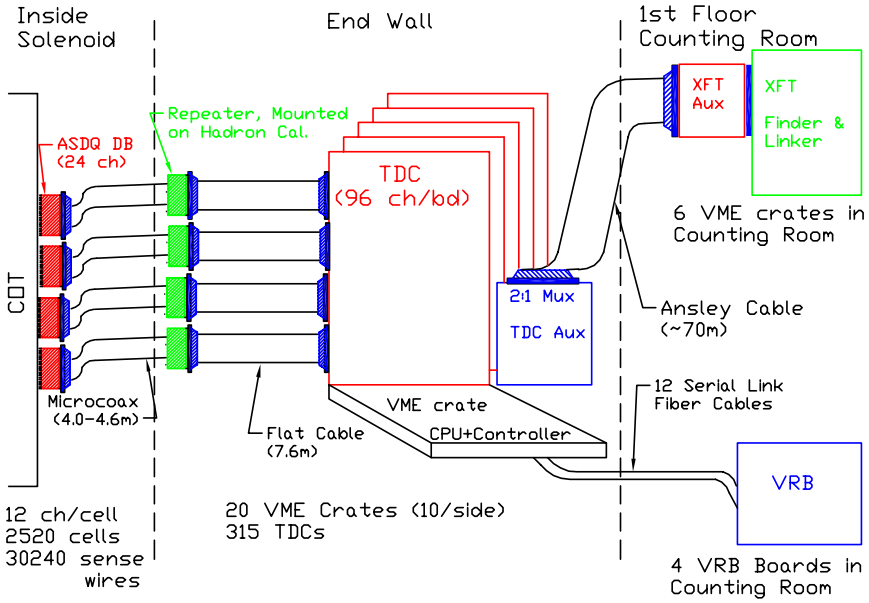

Figure 22. COT read out chain. The figure is divided into sections corresponding to components located inside the solenoid, on the End Wall [East (West) End Wall for superlayers 1, 4, 5, 8 (2, 3, 6, 7)], and in the first floor counting room.

Figure 23. The ASDQ daughter board is shown inserted into the ASDQ motherboard. The three ASDQ chips are the largest ones on the daughter board.

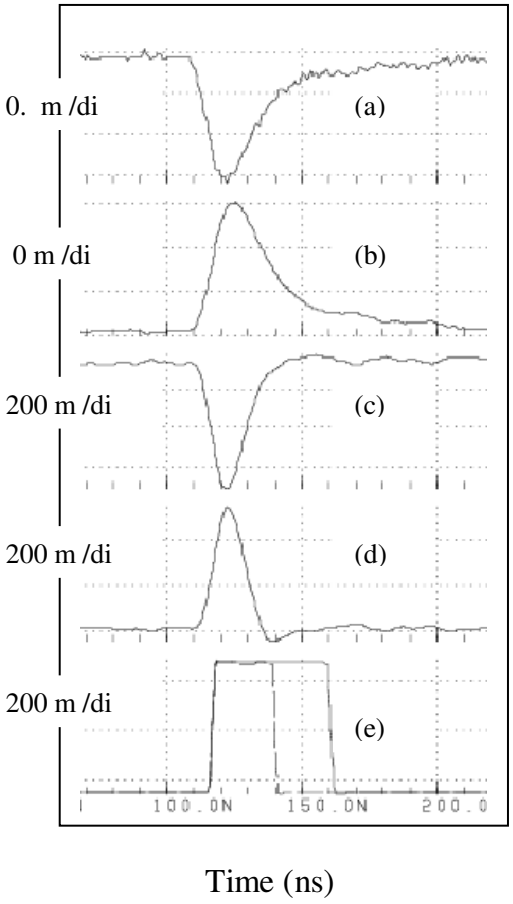

Figure 24. An ~80 fC pulse at the ASDQ a) preamplifier input, b) preamplifier output, c) shaper output, d) BLR output and e) discriminator output (dE/dx off and on).

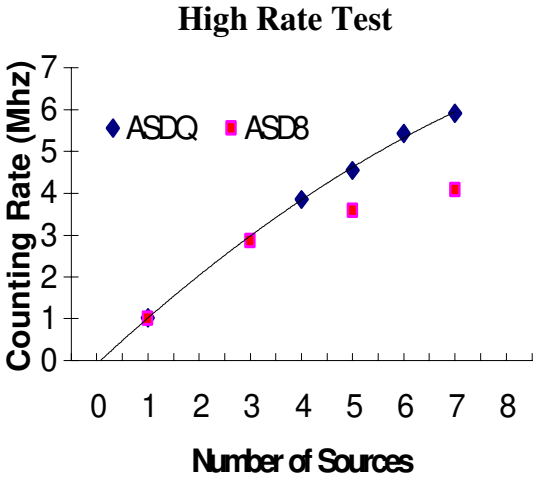

Figure 25. The counting rate on a wire in the High Rate prototype as a function of the number of sources when using the ASD8 no baseline restoration) and the ASDQ. The curve is a polynomial fit through the ASDQ points.

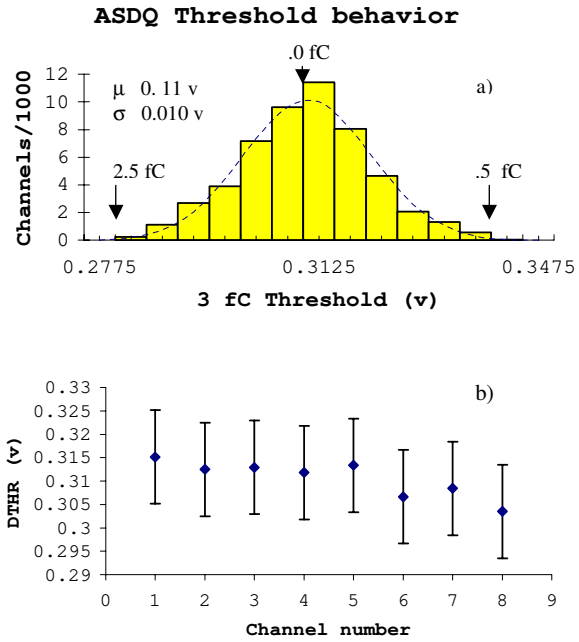

Figure 26. The distribution of 50% trigger rate thresholds for a fC charge for ~6600 ASDQ channels. The charge calibration is 60 mV/fC. Figure a) shows the thresholds for all channels of all chips along with the results of a fit to a Gaussian distribution with mean μ and standard deviation σ. Figure b) shows the average threshold as a function of channel within the chip. The error bar is the standard deviation of the distribution.

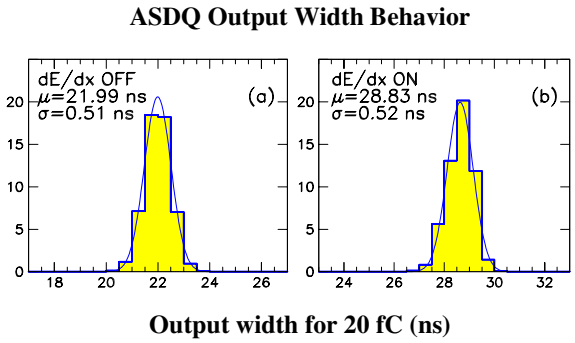

Figure 27. The distribution of output widths for ~6600 ASDQ channels for an injected charge of 20 fC and a) dE/dx off and b) dE/dx on. The vertical scale is channels / 1000. The variation as a function of channel number within the chip is much less than σ.

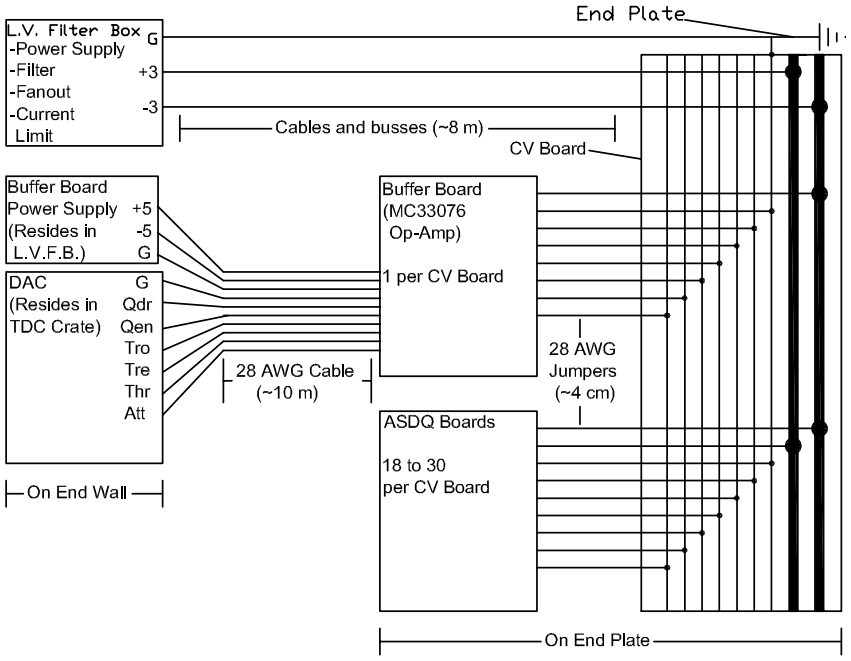

2. b f w w d f h d h b d h d V b d.

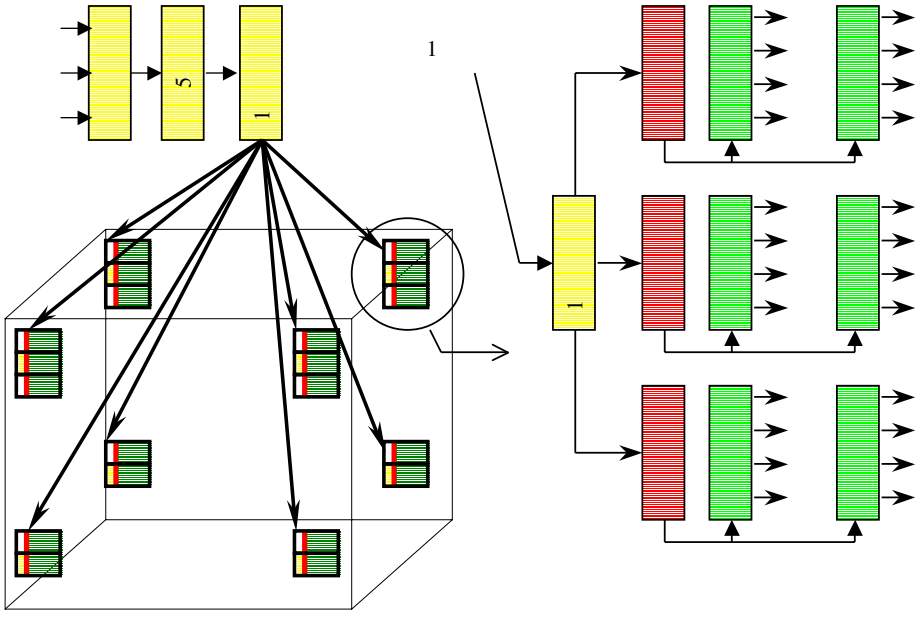

2. b w f h O.

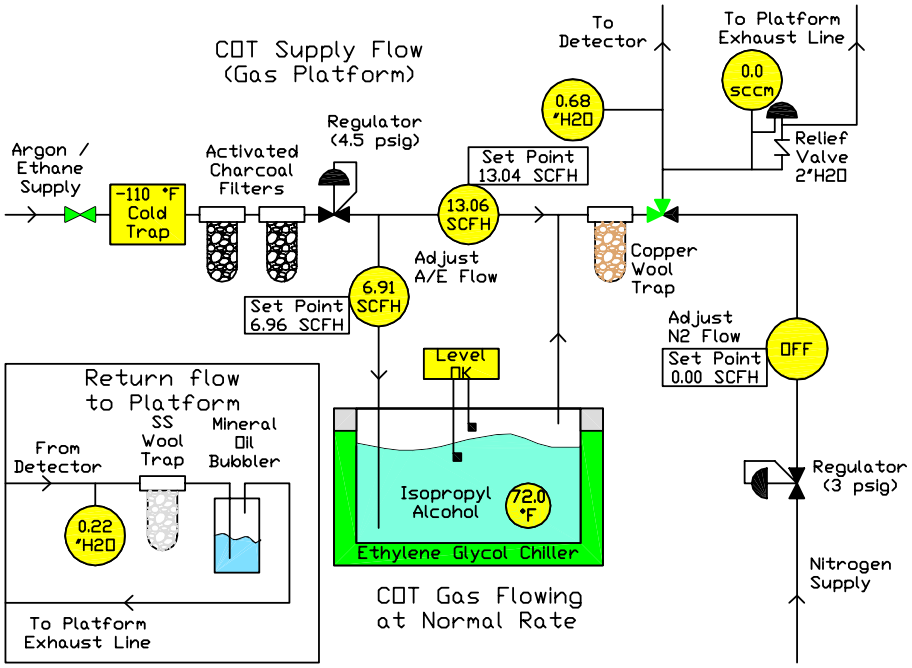

Figure 30. COT drift gas system on the CDF Gas Platform. This is a snapshot of the iFix control and monitor page during normal 20 SCFH flow of argon / ethane.

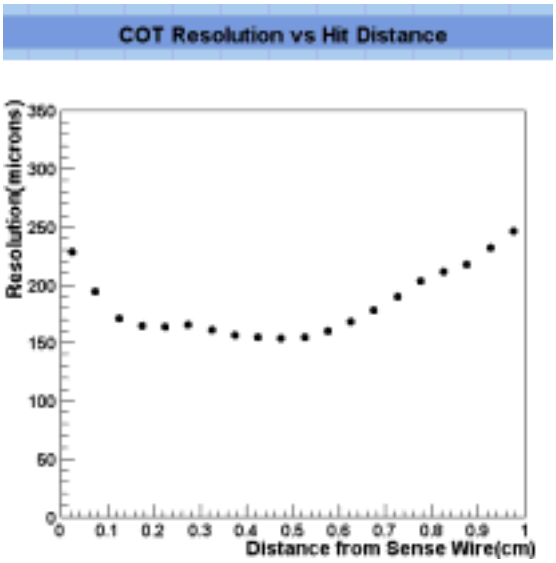

Figure 31. Hit resolution as a function of drift distance measured by the STAGE0 program using data from proton – antiproton collisions.

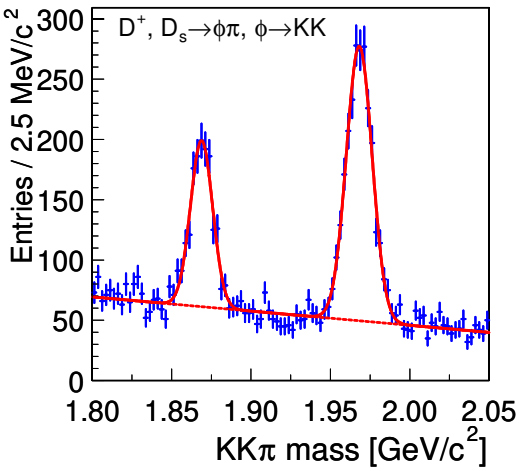

Figure 32. Early Run 2 data showing the D^+ and D_s resonances. The resonances were fit to a Gaussian distribution with $\sigma = 7.7$ MeV.

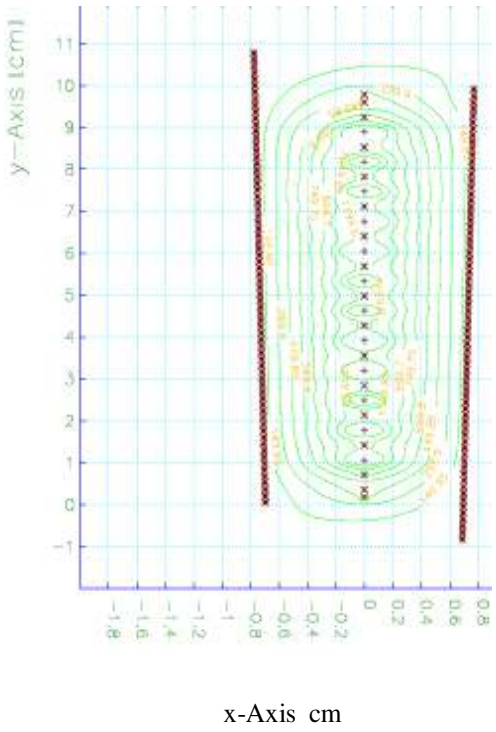

Figure 33. Contours of equal potential in the COT drift cell. Note that the scale of the x-Axis is expanded compared to the y-Axis for clarity. Sense wires: +. Potential wires: x.

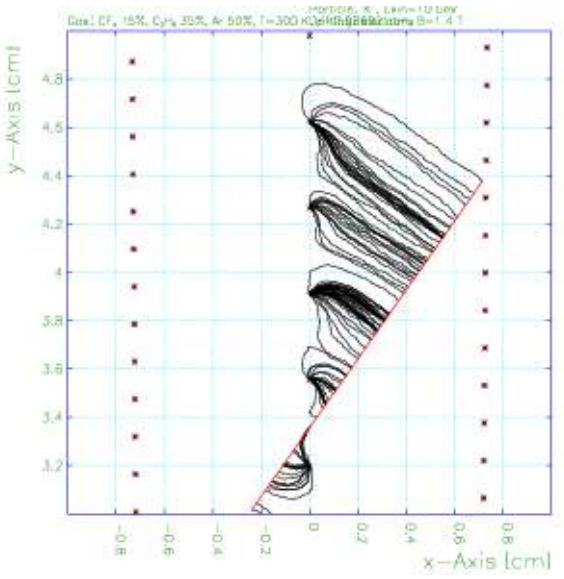

Figure 34. Drift trajectories for a radial (high momentum) track as simulated by GARFIELD and MAGBOLTZ. The cell is set up for a drift field of 2.5 kV/cm and a Lorentz angle of 35° in Argon / Ethane / CF_4 (50:35:15).

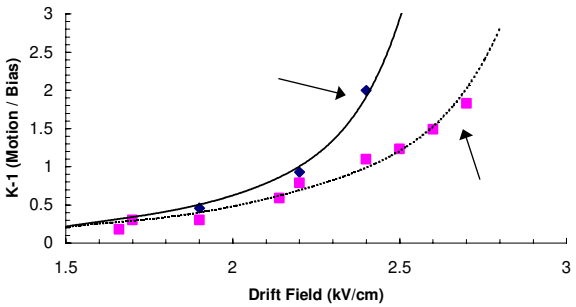

Fig 35. Th ai f h wi la 's l c s a ic m i h bias as a f c i f h d if fi ld. Da a a sh w si g fi ld la s wi h a d wi h a c s . Th c v s a fi s a m d l d sc ibi g h l c s a ic m i .

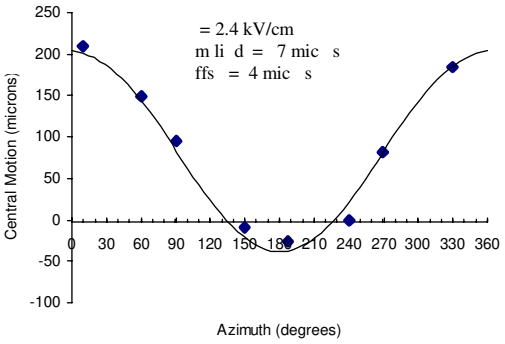

Fig 37. M i f h wi la a z = 0 wh h fi ld is i c as d f m 0 2.4 kV/cm as a f c i f azim h. Th m i is alwa vs m as d wi h s c h sam fi ld la .

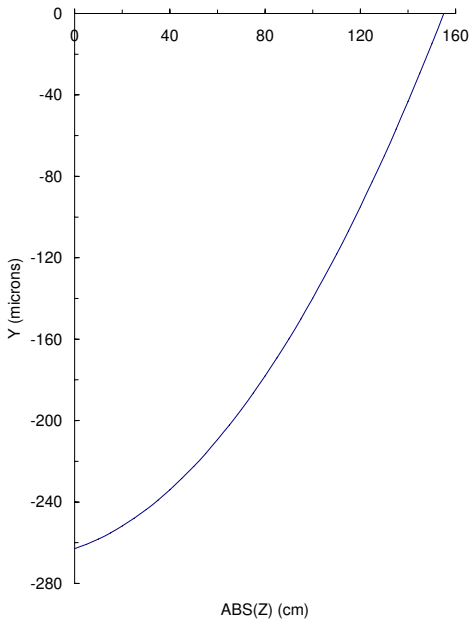

Fig 36. G avi a i al sag f a T wi as a f c i f h abs l val f z.

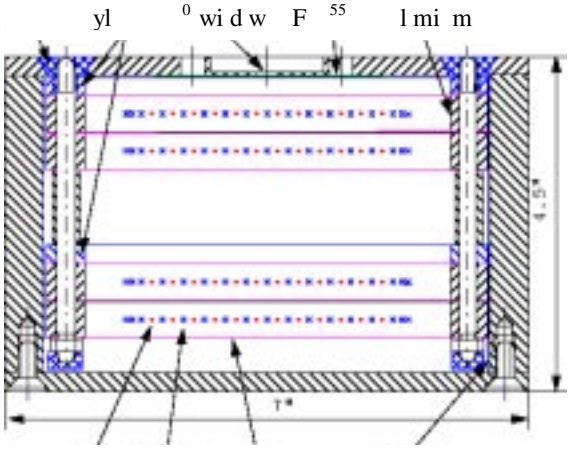

Fig 3 . Th Gas M i hamb s d m i h agi g a a s v al si i si h T gas dis ib i sys m. F m b m, h la s a mb d 4. Th a i s f c s (.g., R =I /I4) a ack d l k f gai l ss i la s – 3 la iv la 4.

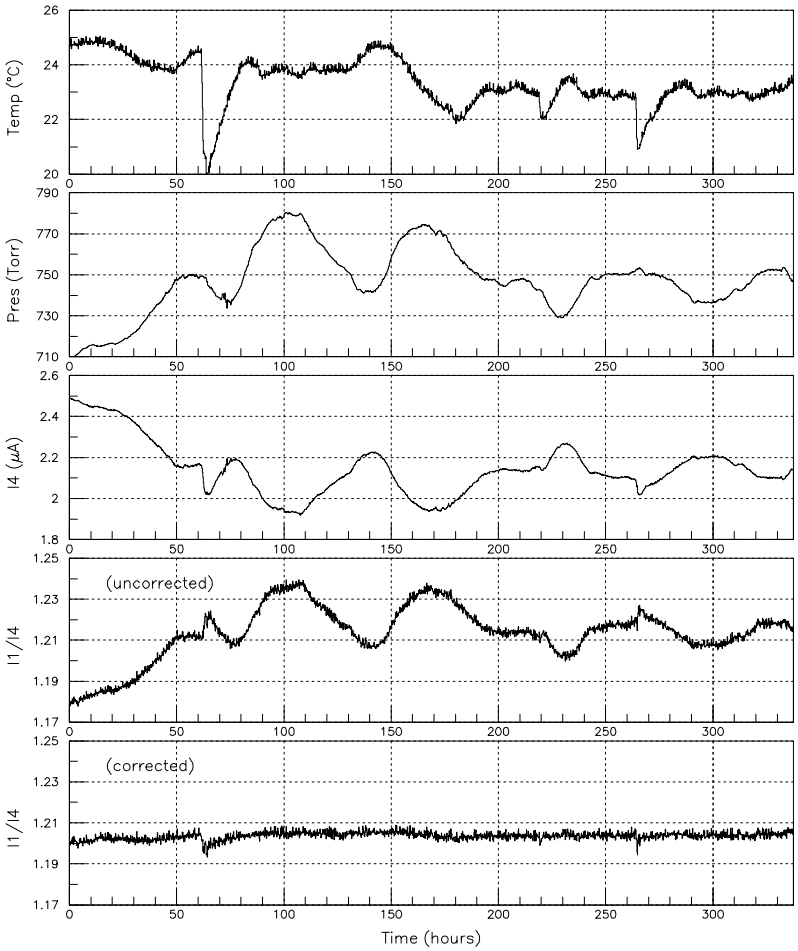

Figure 39. A typical measurement of the current ratio R1 = I1/I4 in the Gas Monitor Chamber as a function of time. The uncorrected ratio is seen to vary with temperature and pressure, but almost all the variation is removed by applying the gas density correction described in the text.